SUPPORTING INFORMATION

In or out? Adaptive metal binding by a diphosphine-based Zr metal-organic cage

Jiehye Shin and Casey R. Wade*

Department of Chemistry and Biochemistry, The Ohio State University, Columbus, Ohio 43210, United States

*Email: wade.521@osu.edu

Table of Contents:

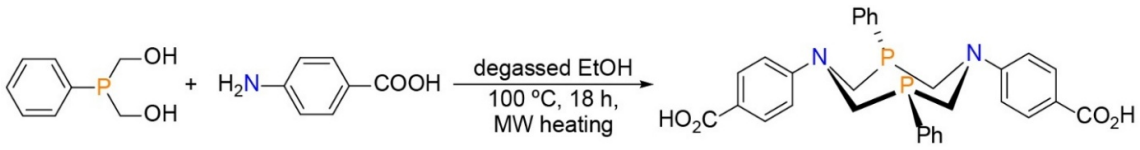

Scheme S1. Synthesis of $H_2(P_2N_2)$.

Table S1. Crystal data and structure refinement for **Zr-P_2N_2**.

Empirical formula	$C_{160}H_{202}Cl_2N_{14}O_{28}P_6Zr_6$
Formula weight	3573.38
Temperature/K	100
Crystal system	orthorhombic
Space group	Fdd2
a/Å	53.629(9)
b/Å	22.341(3)
c/Å	29.820(5)
α/°	90
β/°	90
γ/°	90
Volume/Å^3	35729(10)
Z	8
ρ_{calc}g/cm^3	1.329
μ/mm^{-1}	0.488
F(000)	14784.0
Crystal size/mm^3	0.3 × 0.15 × 0.1
Radiation	MoKα (λ = 0.71073)
2Θ range for data collection/°	3.95 to 34.54
Index ranges	-44 ≤ h ≤ 44, -18 ≤ k ≤ 18, -24 ≤ l ≤ 24
Reflections collected	165892
Independent reflections	5462 [R_{int} = 0.2086, R_{sigma} = 0.0534]
Data/restraints/parameters	5462/917/628
Goodness-of-fit on F^2	1.036
Final R indexes [I>=2σ (I)]	R_1 = 0.0531, wR_2 = 0.1354
Final R indexes [all data]	R_1 = 0.0686, wR_2 = 0.1471
Largest diff. peak/hole / e Å^{-3}	0.63/-0.31
Flack parameter	0.42(10)

A solvent mask was calculated, and 3715 electrons were found in a volume of 15784 Å^3 in 2 voids per unit cell. This is consistent with the presence of 64 [$C_5H_{11}NO$ (DEF)], which accounts for 3584 electrons per unit cell.

Due to the significant solvent disorder, a precise determination of the solvent occupancy within the cavities via direct refinement was impossible. However, we estimated the solvent content by modeling the residual electron density (Q peaks) as DEF molecules with free chemical occupancy and applying the SQUEEZE procedure to the interstitial Q peaks. Through this method, 2310 electrons (12860 Å^3 in 3 voids) were identified as interstitial electrons per unit cell, which is consistent with the presence of 56 DEF molecules (2560 electrons). Given there are 8 cages per unit cell, this indicates that approximately one DEF molecule resides inside each cage cavity.

Table S2. Bond angles around the N atoms in **Zr-P_2N_2**.

Nitrogen atoms	Angle		Sum (average)
N1	C20–N1–C24	124.99 º	359.98 º (119.99 º)
	C23–N1–C20	119.06 º	
	C24–N1–C23	115.93 º	
N2	C38–N2–C39	111.61 º	359.84 º (119.95 º)
	C39–N2–C35	124.42 º	
	C38–N2–C35	123.81 º	
N3	C54–N3–C40	125.46 º	359.73 º (119.91 º)
	C40–N3–C41	116.86 º	
	C54–N3–C41	117.41 º	

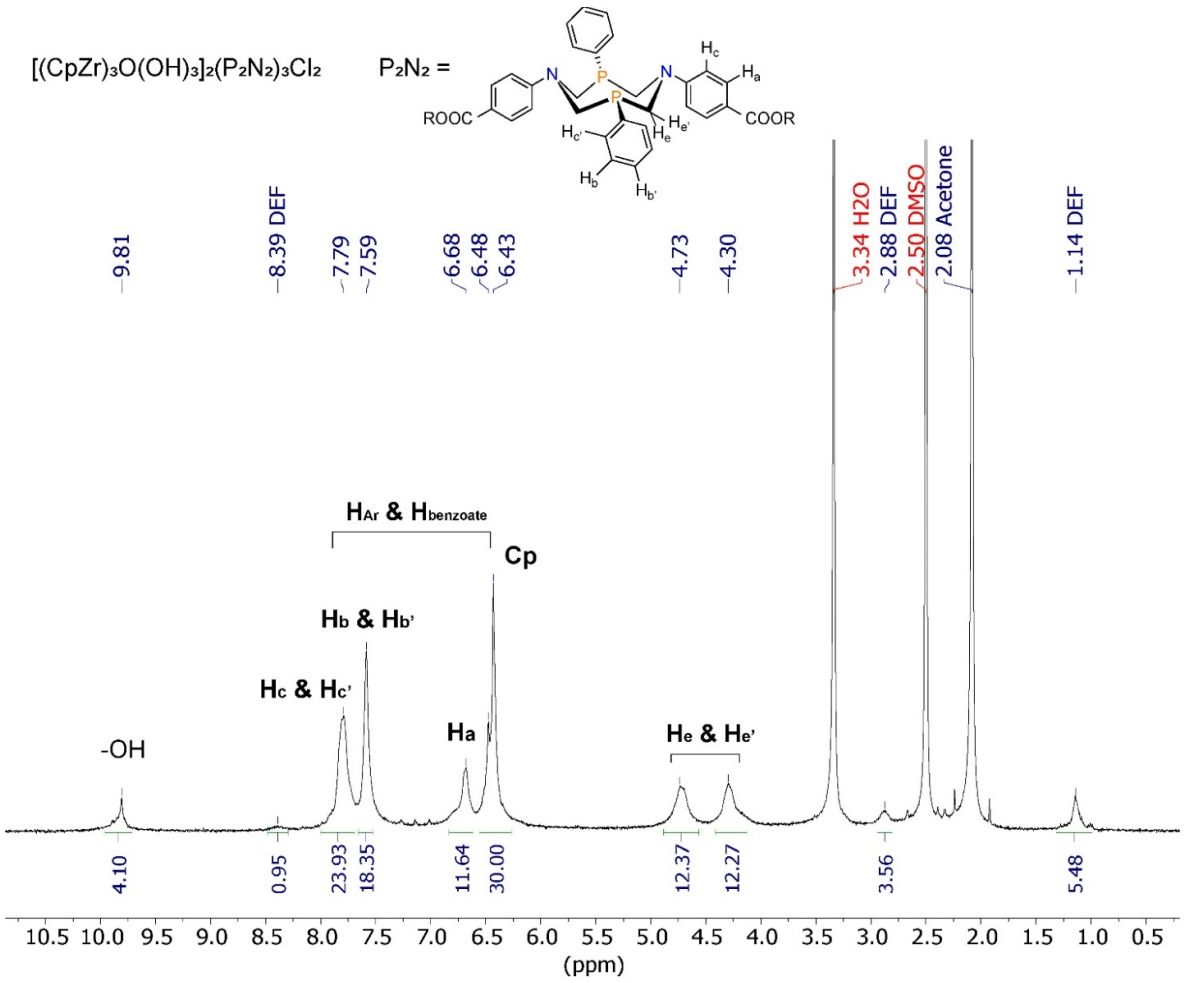

Figure S1. ^{1}H NMR spectrum of **Zr-P_2N_2** (DMSO-d_6, 400 MHz).

Zr-P_2N_2 was washed with acetone to remove DEF solvent molecules in the interstitial space between the cages. The spectrum shows the presence of ~1 remaining DEF molecule per cage.

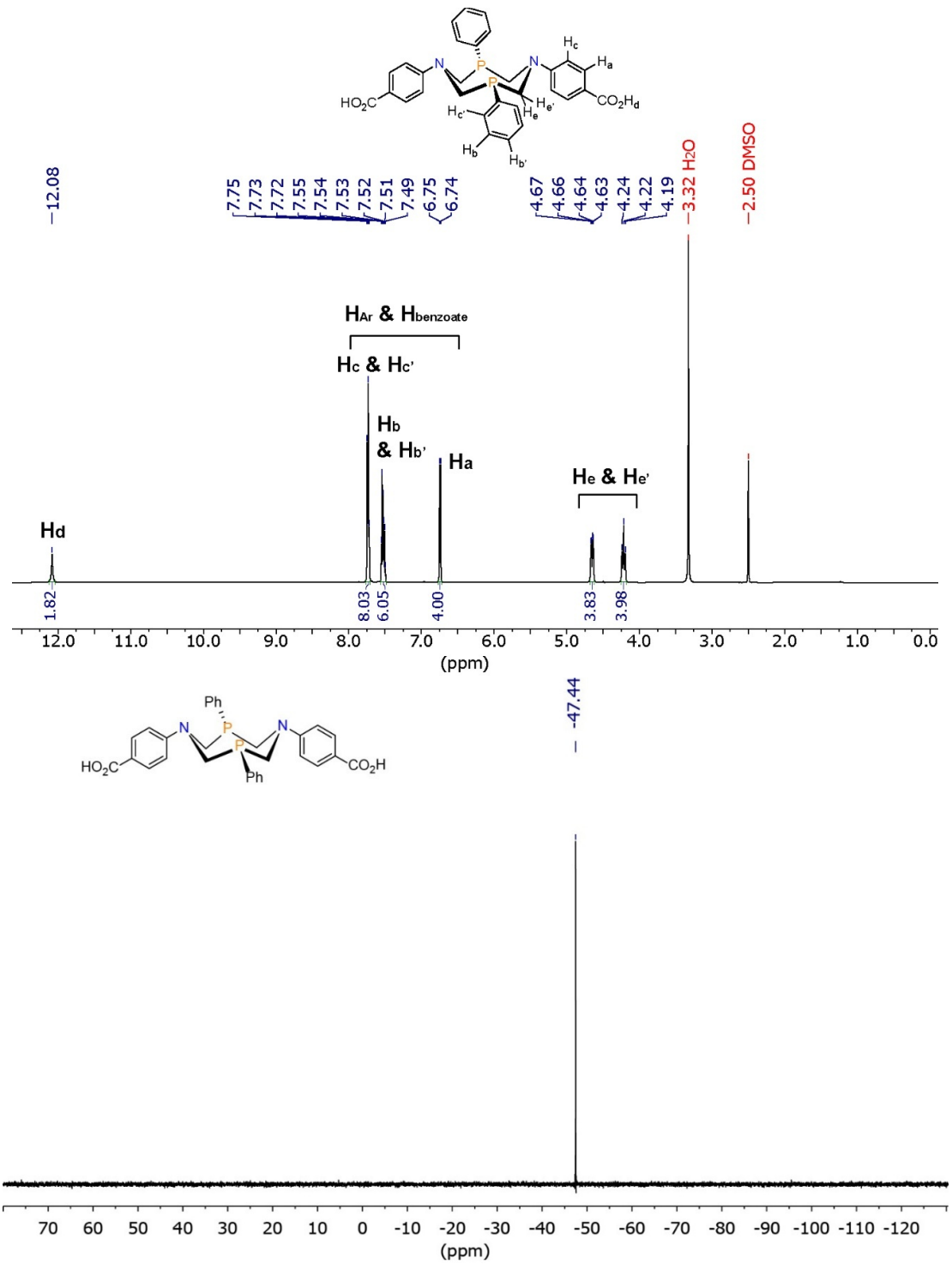

Figure S2. ^{1}H and $^{31}P\{^{1}H\}$ NMR spectra of $H_2(P_2N_2)$.

(DMSO-d_6, 600 MHz and 162 MHz)

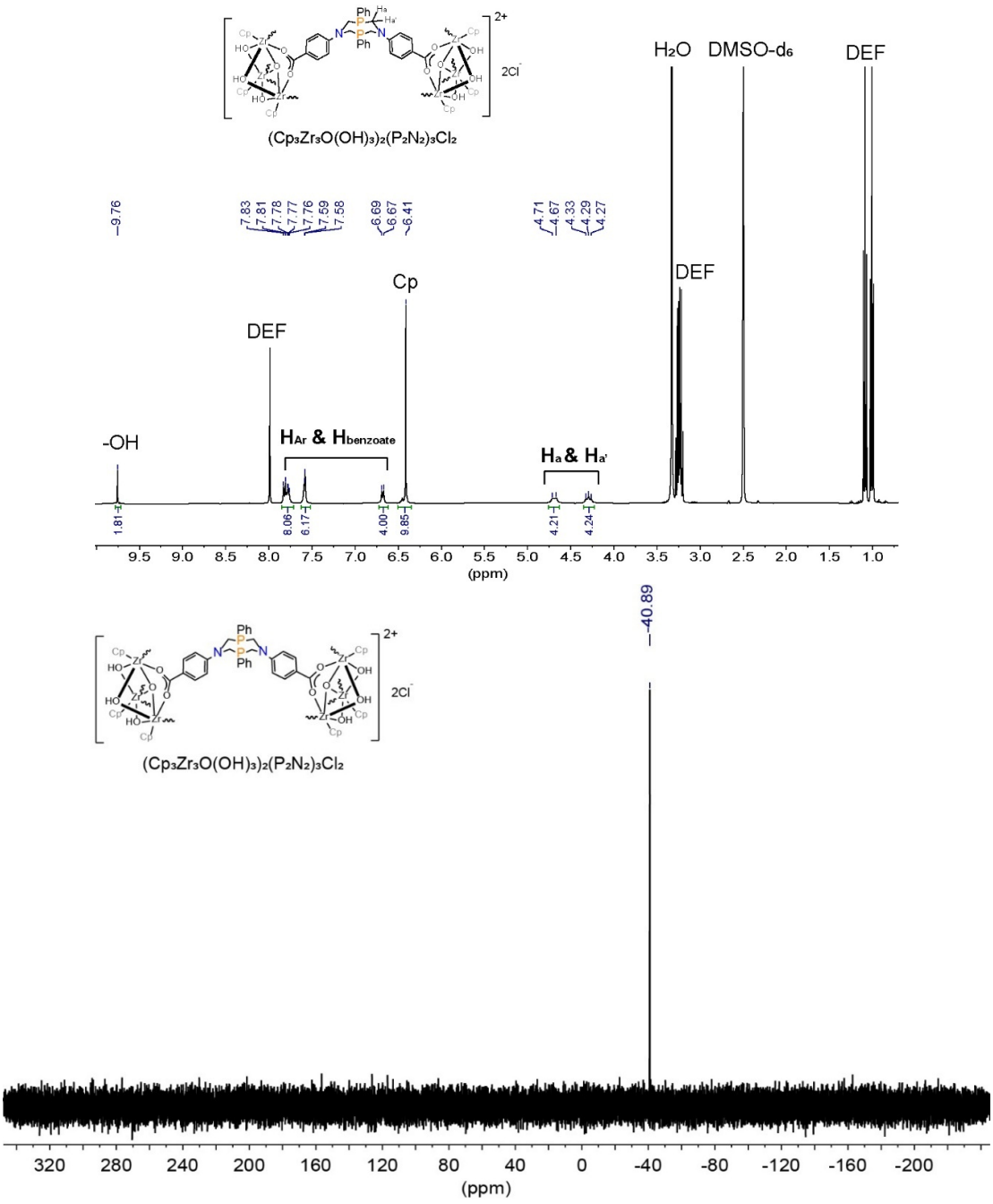

Figure S3. ^{1}H and $^{31}P\{^{1}H\}$ NMR spectra of **Zr-P_2N_2**.
(DMSO-d_6, 400 MHz and 162 MHz)

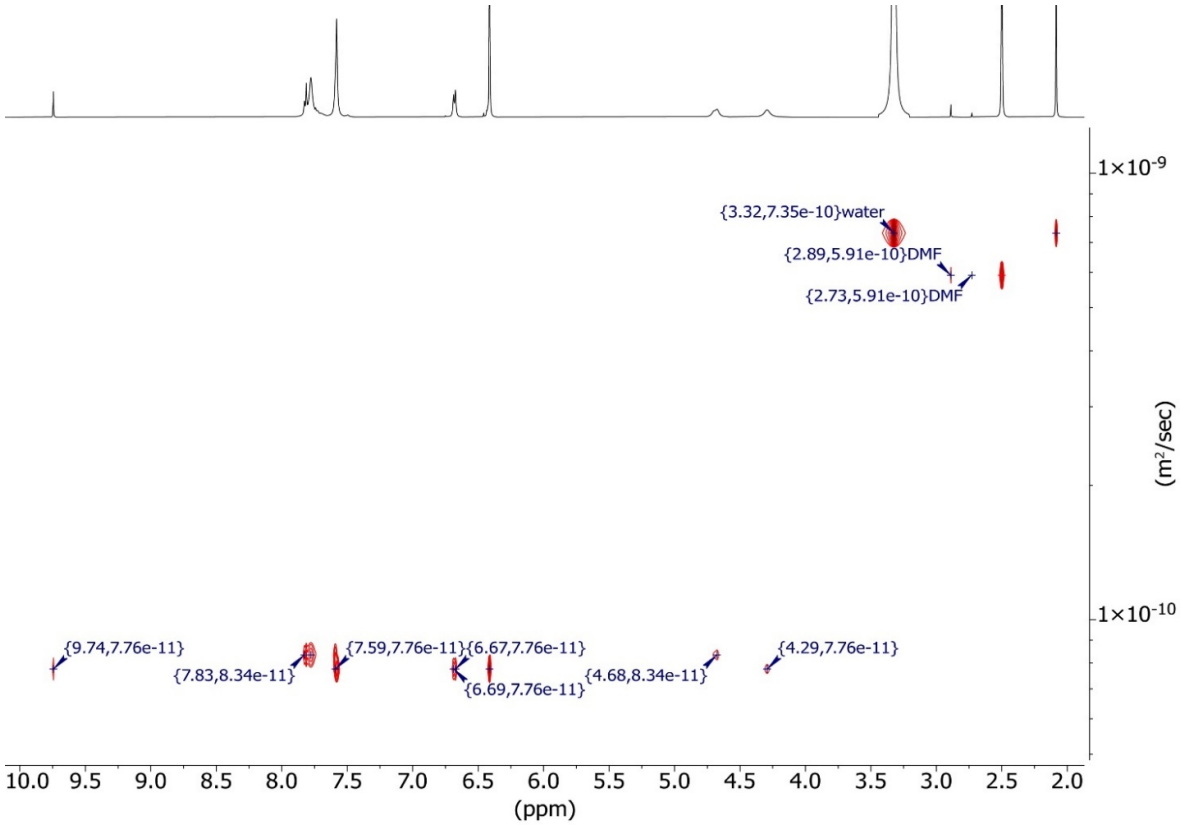

Figure S4. ^{1}H DOSY NMR spectrum of **Zr-P$_2$N$_2$** in DMSO-d_6

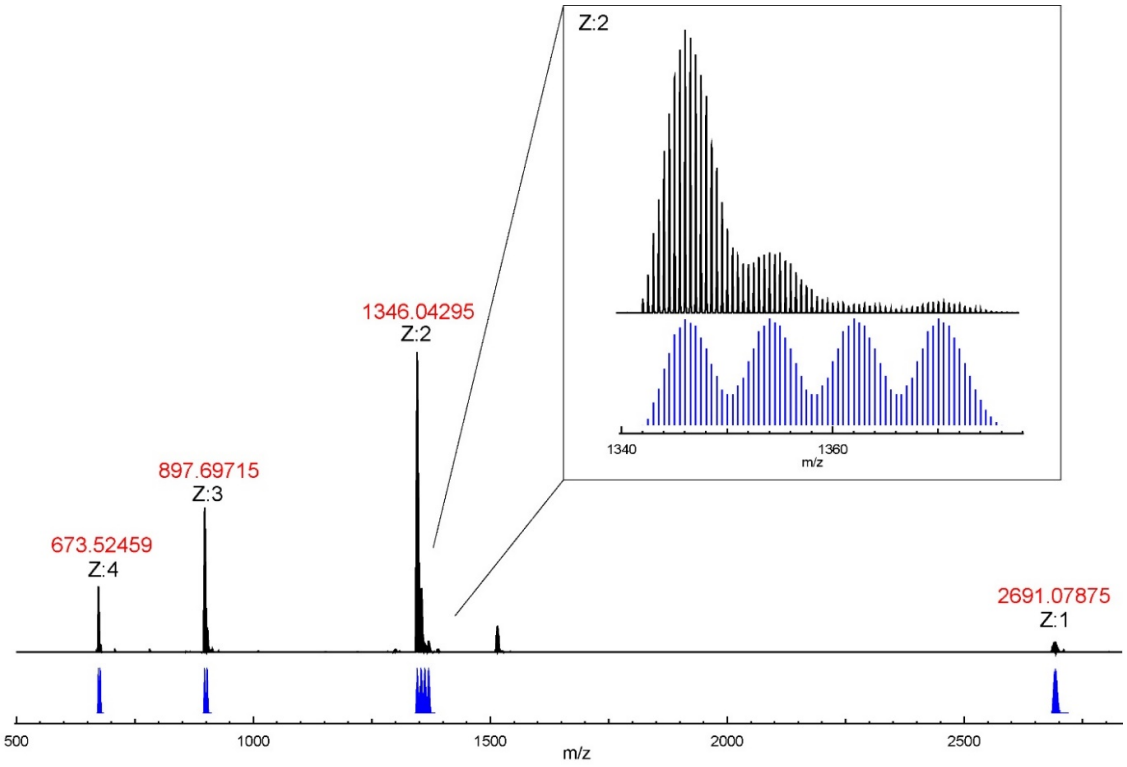

Assignments	m/z experimental	m/z simulated
$(C_{120}H_{113}N_6O_{20}P_6Zr_6)^{+}$	2691.07875	2691.07795
$(C_{120}H_{114}N_6O_{20}P_6Zr_6)^{2+}$ $\{[(ZrCp)_3O(OH)_3]_2(P_2N_2)_3\}^{2+}$	1346.04295	1346.04266
$(C_{120}H_{114}N_6O_{21}P_6Zr_6)^{2+}$	1354.04075	1354.04012
$(C_{120}H_{114}N_6O_{22}P_6Zr_6)^{2+}$	1362.04482	1362.03758
$(C_{120}H_{114}N_6O_{23}P_6Zr_6)^{2+}$	1370.05229	1370.03504
$(C_{120}H_{115}N_6O_{20}P_6Zr_6)^{3+}$	897.69715	897.69753
$(C_{120}H_{115}N_6O_{21}P_6Zr_6)^{3+}$	902.69602	903.02917
$(C_{120}H_{116}N_6O_{20}P_6Zr_6)^{4+}$	673.52459	673.52497
$(C_{120}H_{116}N_6O_{21}P_6Zr_6)^{4+}$	677.52366	677.52370

Sample was dissolved in methanol and measured in positive mode with m/z from 200 to 3000.

Figure S5. Simulated and experimental ESI-MS spectra of **Zr-P_2N_2.**

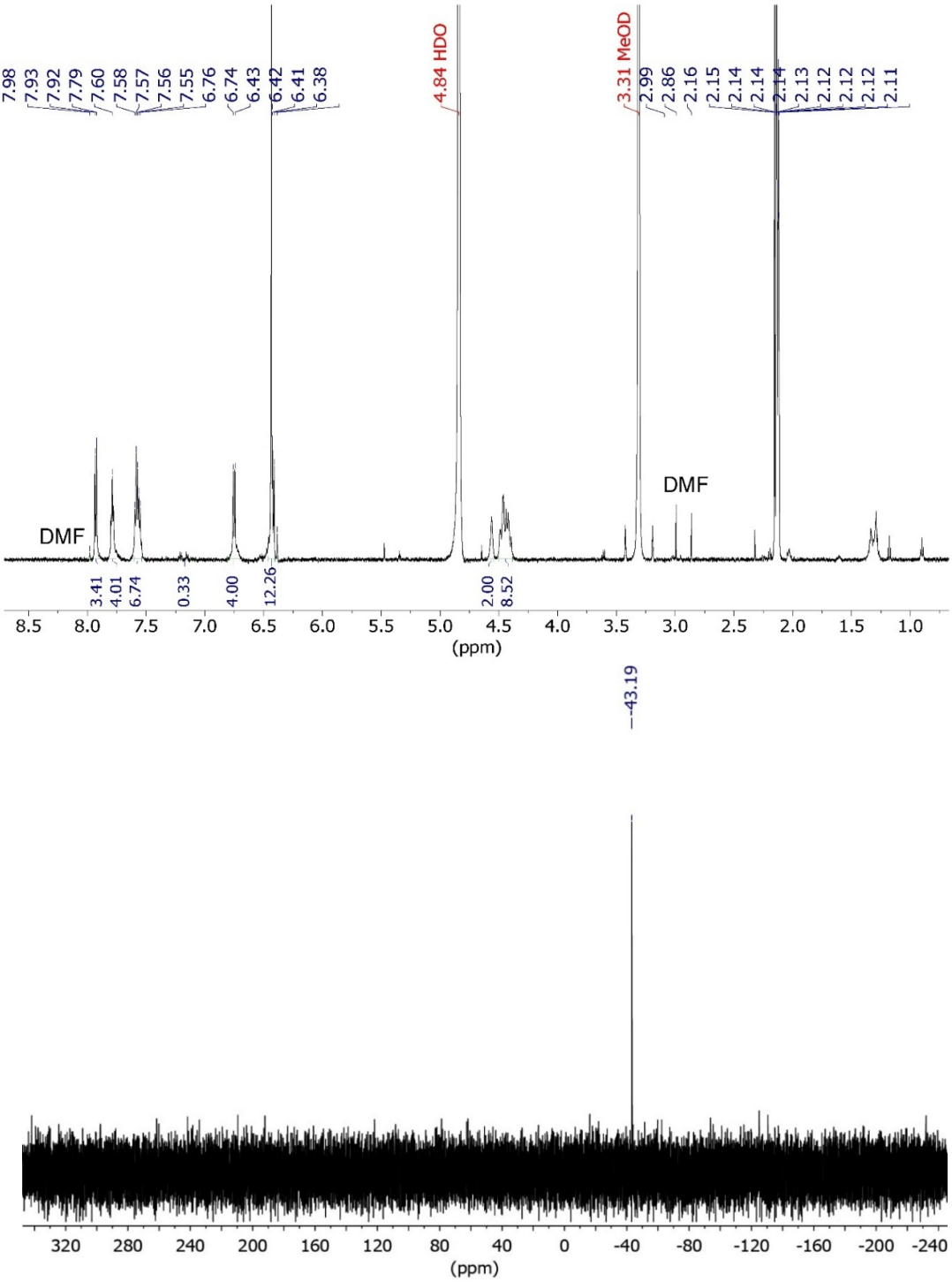

Figure S6. ^{1}H and ^{31}P{^{1}H} NMR spectra of **Zr-P$_2$N$_2$** in MeOD-d_4.

(400 MHz and 162 MHz).

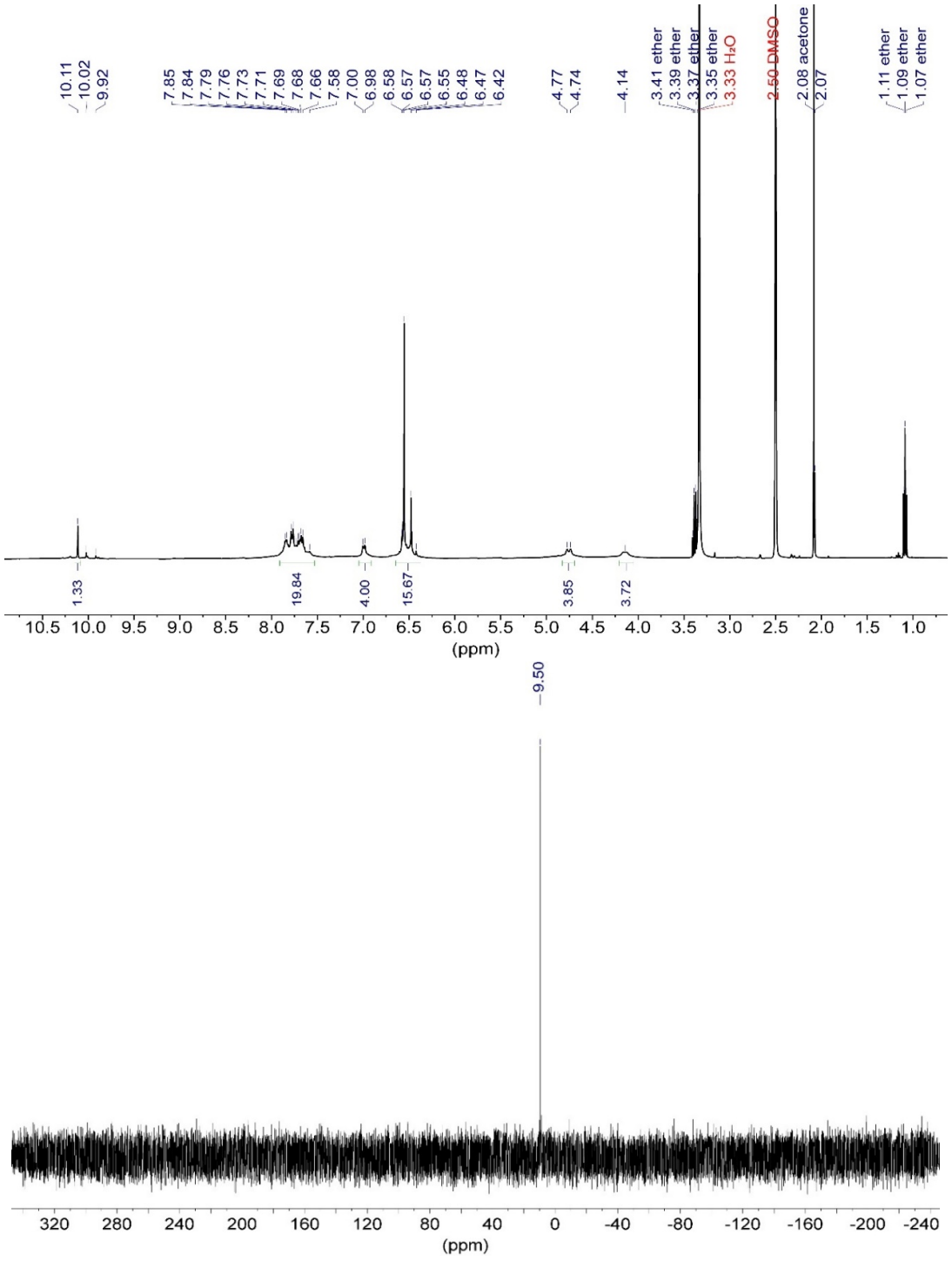

Figure S7. ^{1}H and $^{31}P\{^{1}H\}$ NMR spectra of **Zr-P_2N_2-$PdCl_2$** from postsynthetic metalation.

(DMSO-d_6, 400 MHz and 162 MHz)

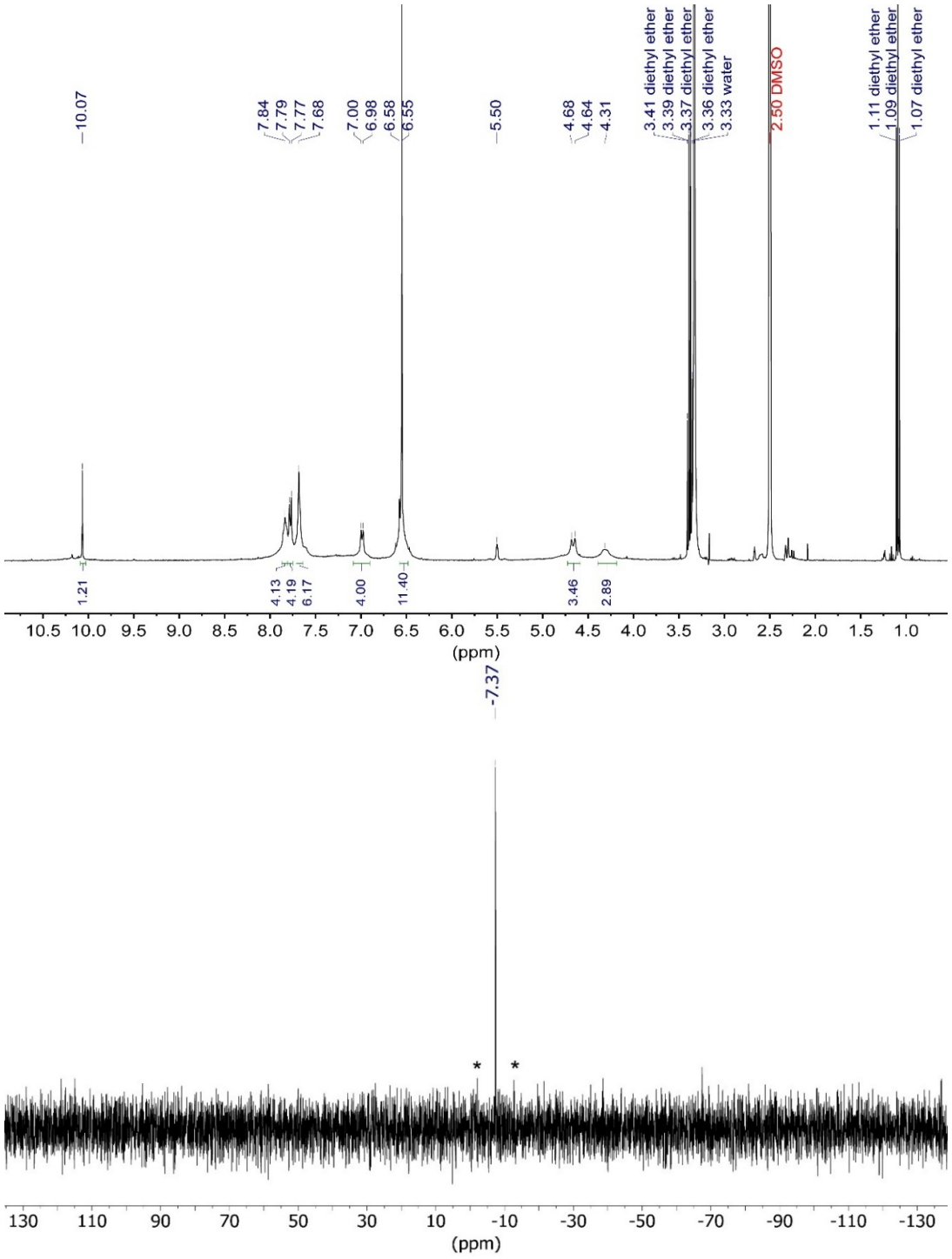

Figure S8. ^{1}H and $^{31}P\{^{1}H\}$ NMR spectra of **Zr-P$_2$N$_2$-PtCl$_2$** from postsynthetic metalation.

(DMSO-d_6, 400 MHz and 243 MHz)

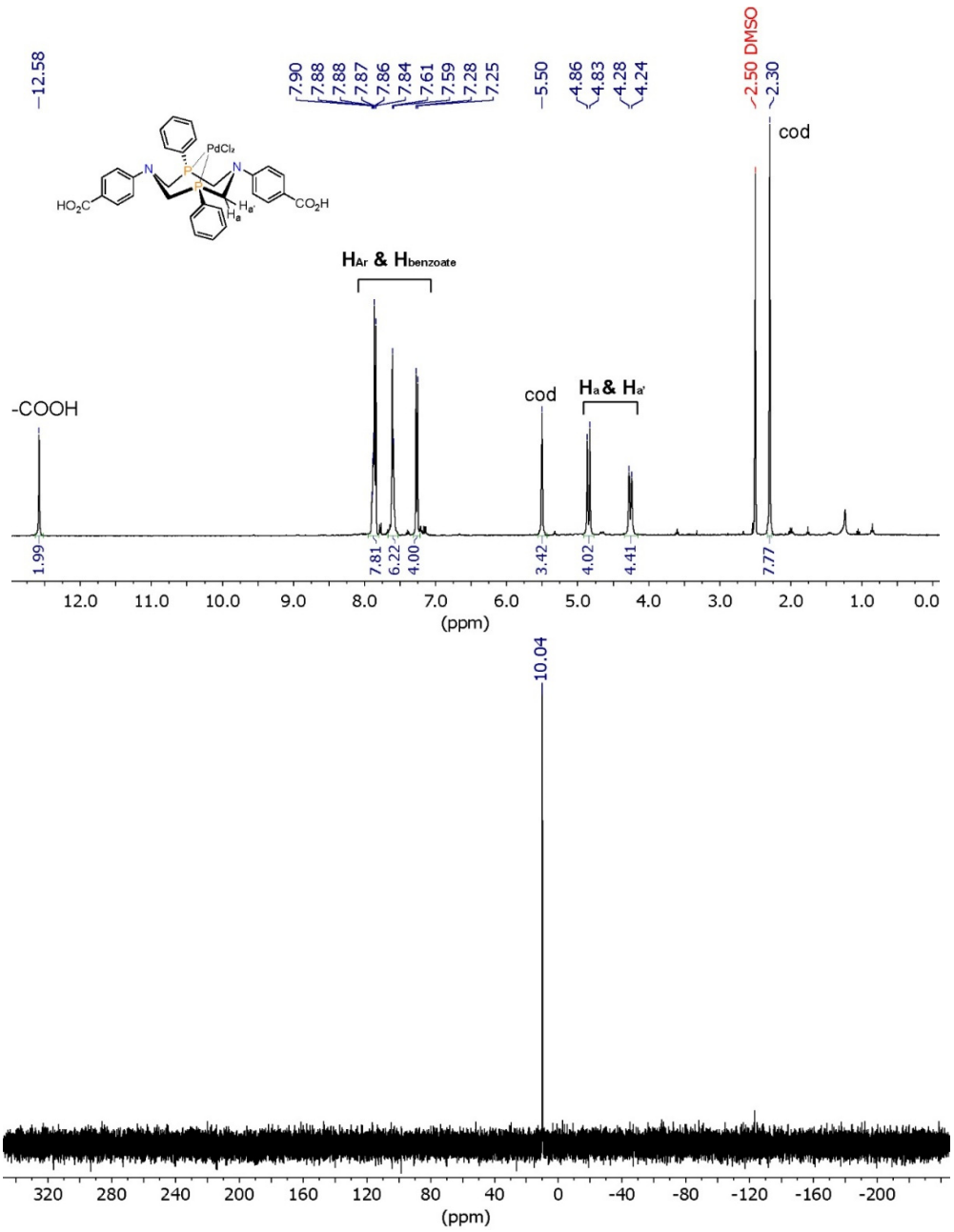

Figure S9. ^{1}H and $^{31}P\{^{1}H\}$ NMR spectra of **$H_2(P_2N_2\text{-}PdCl_2)$** generated *in situ* by mixing **$H_2(P_2N_2)$** and $PdCl_2$(cod).
(DMSO-d_6, 400 MHz and 162 MHz)

$H_2(P_2N_2\text{-}PdCl_2)$ was prepared in situ by dissolving $H_2(P_2N_2)$ (3 mg, 0.006 mmol) and $PdCl_2$(cod) (2 mg, 0.006 mmol) in 1 mL of DMSO-d_6. ^{1}H NMR (400 MHz, DMSO-d_6) δ 12.58 (s, 2H), 7.90 – 7.84 (m, 8H), 7.61-7.59 (m, 6H), 7.27 (d, $^{2}J_{H-H}$= 9.1 Hz, 4H), 4.85 (d, $^{2}J_{H-H}$ = 14.5 Hz, 4H), 4.26 (d, $^{2}J_{H-H}$ = 14.8 Hz, 4H). $^{31}P\{^{1}H\}$ NMR (162 MHz, DMSO-d_6) δ 10.04.

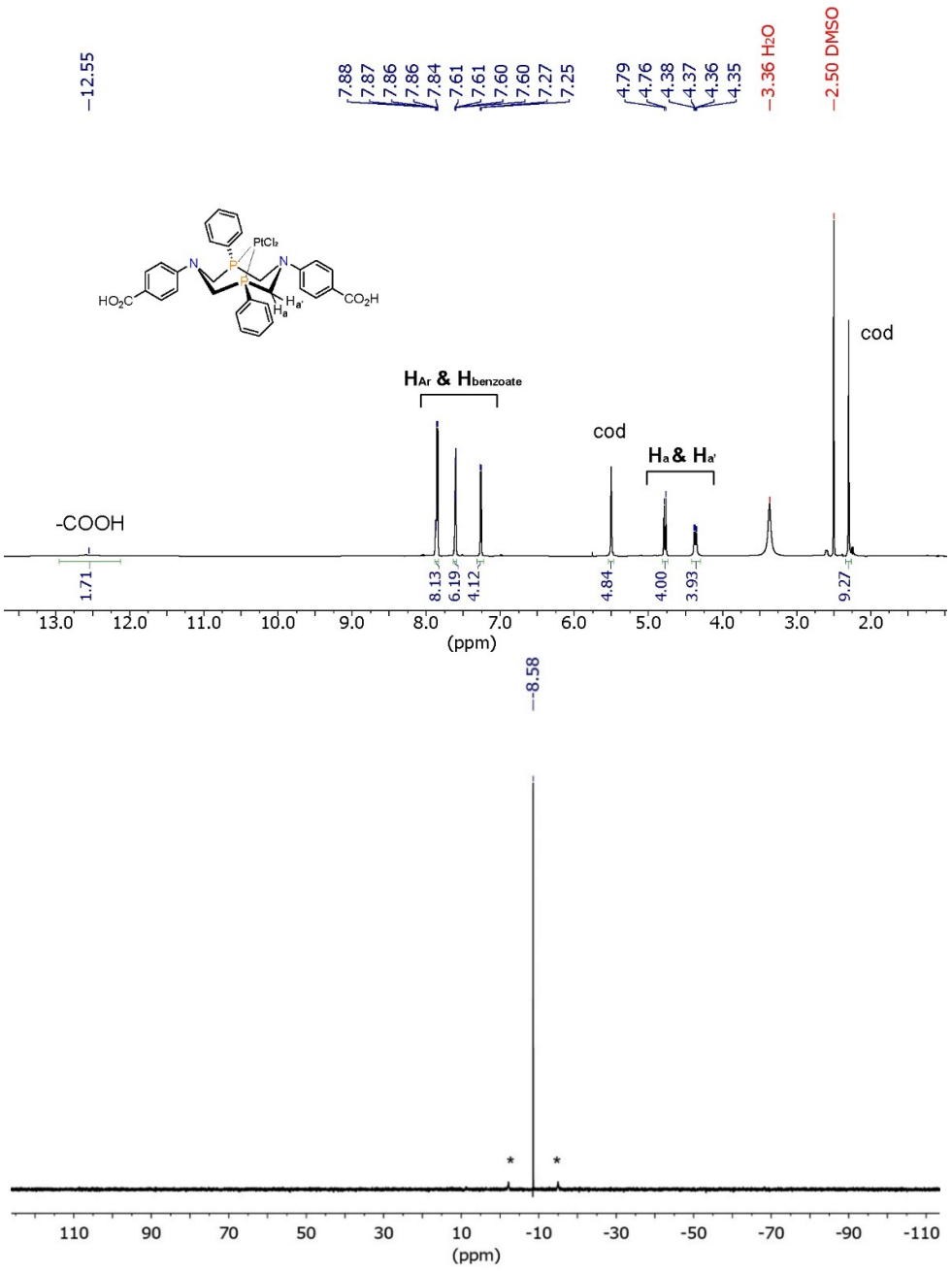

Figure S10. ^{1}H and $^{31}P\{^{1}H\}$ NMR spectra of **$H_2(P_2N_2\text{-}PtCl_2)$** generated *in situ* by mixing **$H_2(P_2N_2)$** and $PtCl_2(cod)$.
(DMSO-d_6, 600 MHz and 243 MHz)

$H_2(P_2N_2\text{-}PtCl_2)$ was prepared in situ by dissolving $H_2(P_2N_2)$ (5 mg, 0.009 mmol) and $PtCl_2(cod)$ (3 mg, 0.009 mmol) in 1 mL of DMSO-d_6. ^{1}H NMR (600 MHz, DMSO-d_6): δ 12.55 (s, 2H), 7.88 – 7.84 (m, 8H), 7.61 – 7.60 (m, 6H), 7.26 (d, $^{2}J_{H-H}$ = 9.2 Hz, 4H), 4.78 (d, $^{2}J_{H-H}$ = 14.6 Hz, 4H), 4.37 (dd, $^{2}J_{H-H}$ = 14.9, $^{2}J_{P-H}$ = 5.7 Hz, 4H). $^{31}P\{^{1}H\}$ NMR (243 MHz, DMSO-d_6) δ -8.58.

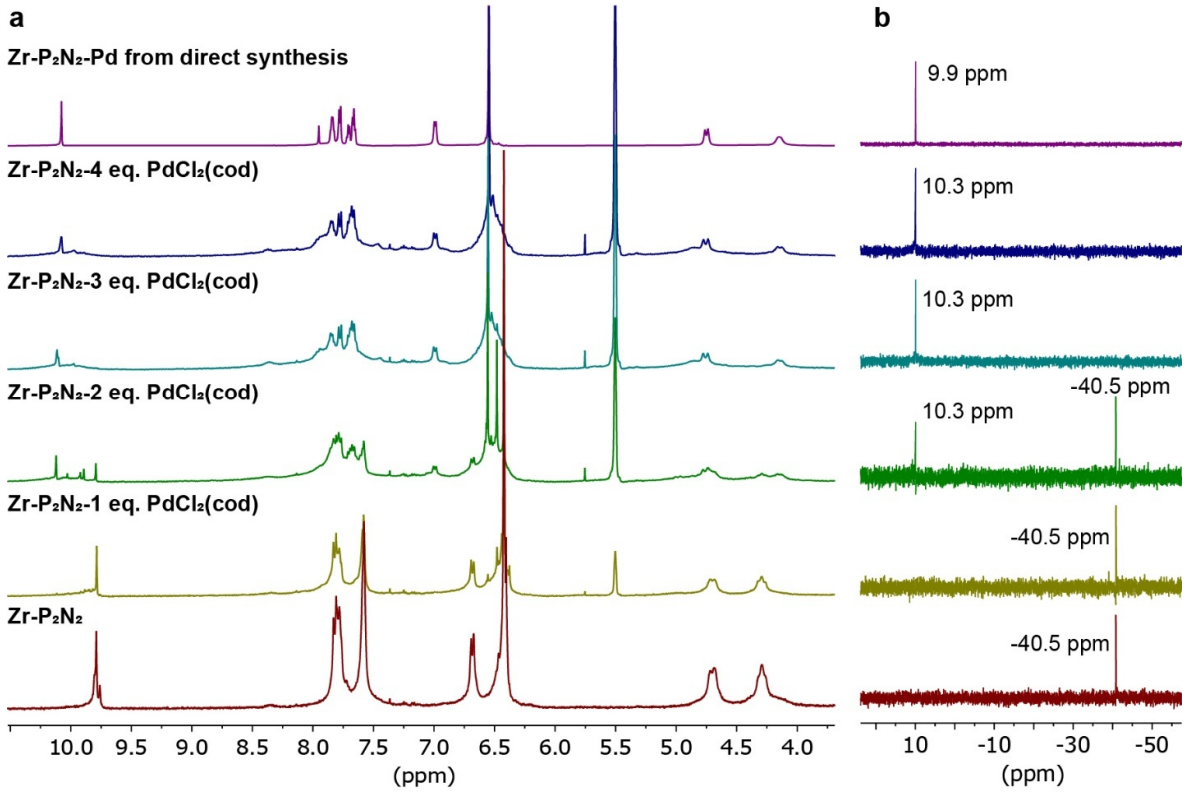

Figure S11. (a) ^{1}H and (b) ^{31}P{^{1}H} NMR spectra of **Zr-P$_2$N$_2$-PdCl$_2$** from direct synthesis and titration.

(DMSO-d_6, 600 MHz and 243 MHz)

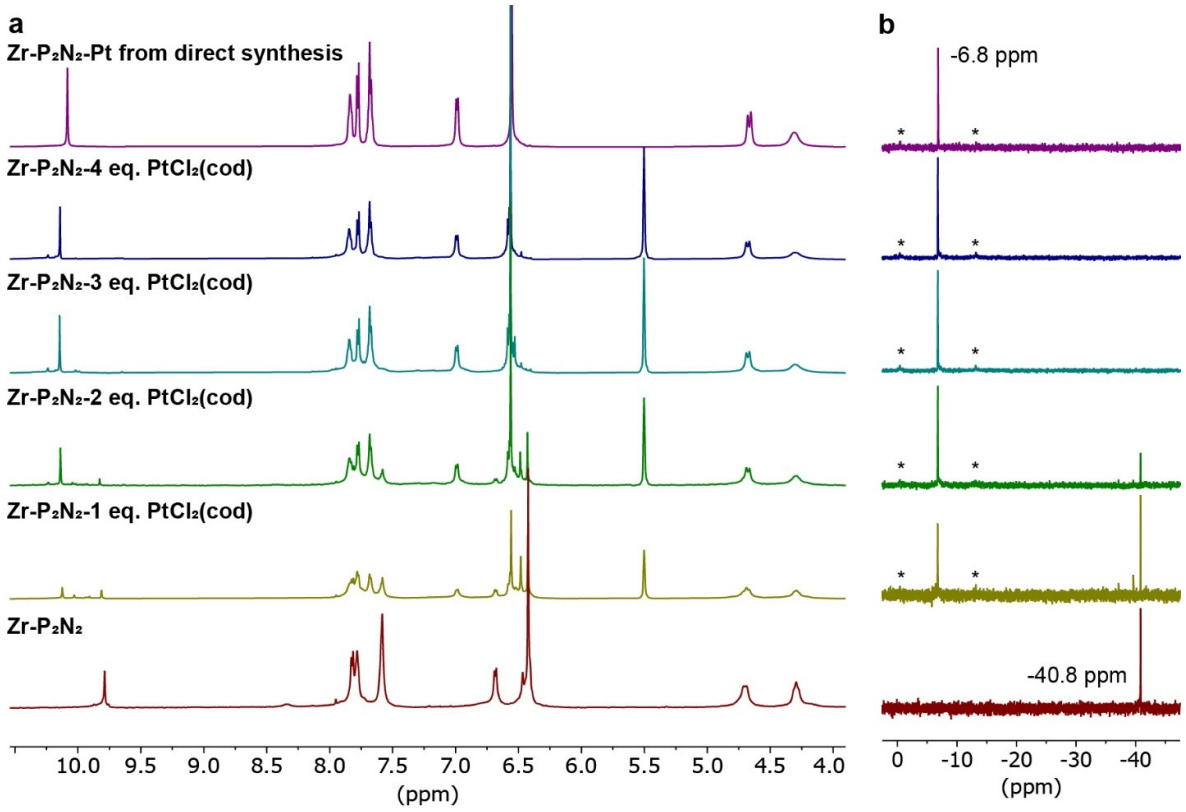

Figure S12. (a) ^{1}H and (b) ^{31}P{^{1}H} NMR spectra of **Zr-P_2N_2-$PtCl_2$** from direct synthesis and titration.

(DMSO-d_6, 600 MHz and 243 MHz)

The * symbol in the ^{31}P NMR spectra denotes "satellites" that result from ^{195}Pt-^{31}P coupling.

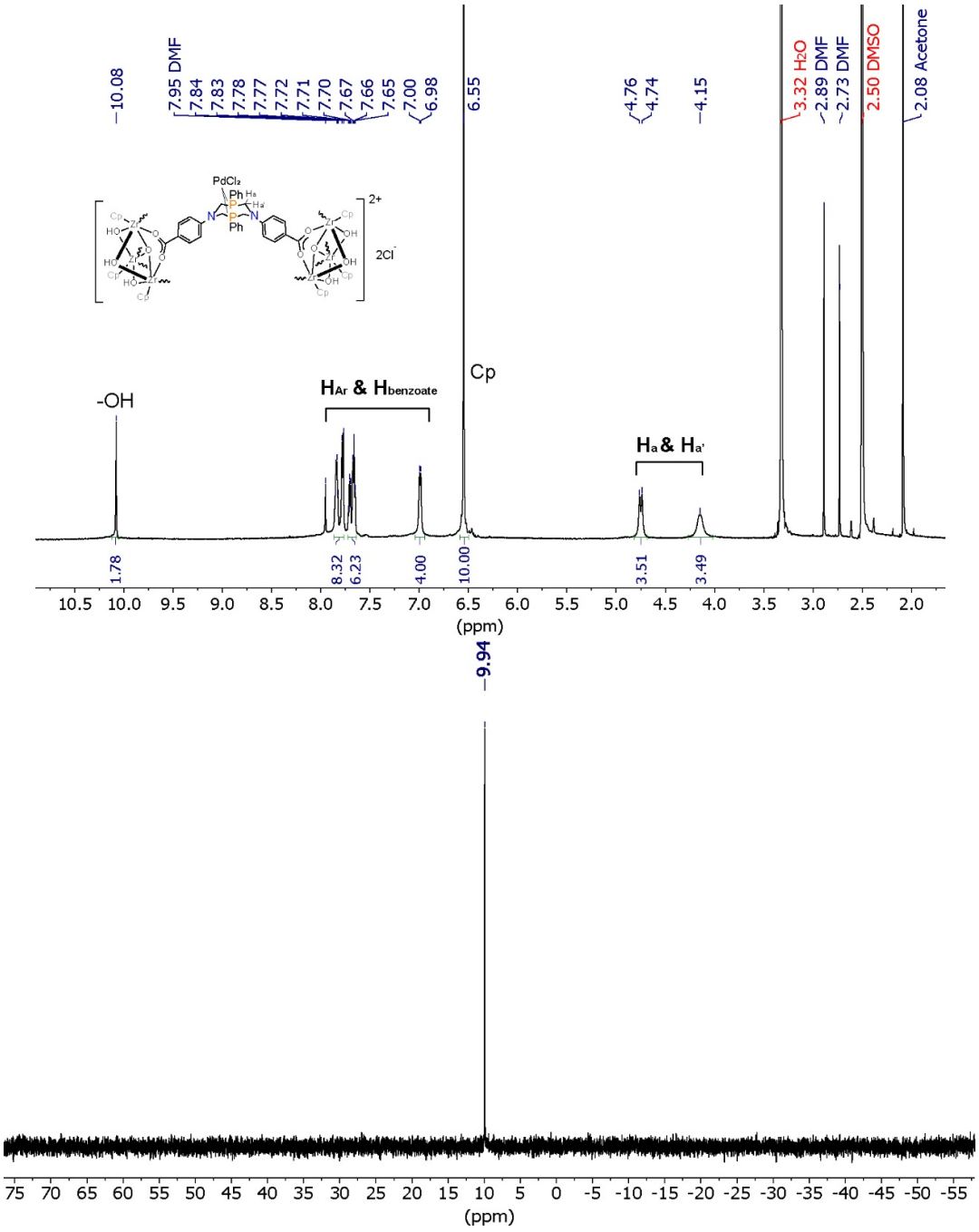

Figure S13. ^{1}H and $^{31}P\{^{1}H\}$ NMR spectra of **Zr-P_2N_2-$PdCl_2$** from direct synthesis.

(DMSO-d_6, 600 MHz and 243 MHz)

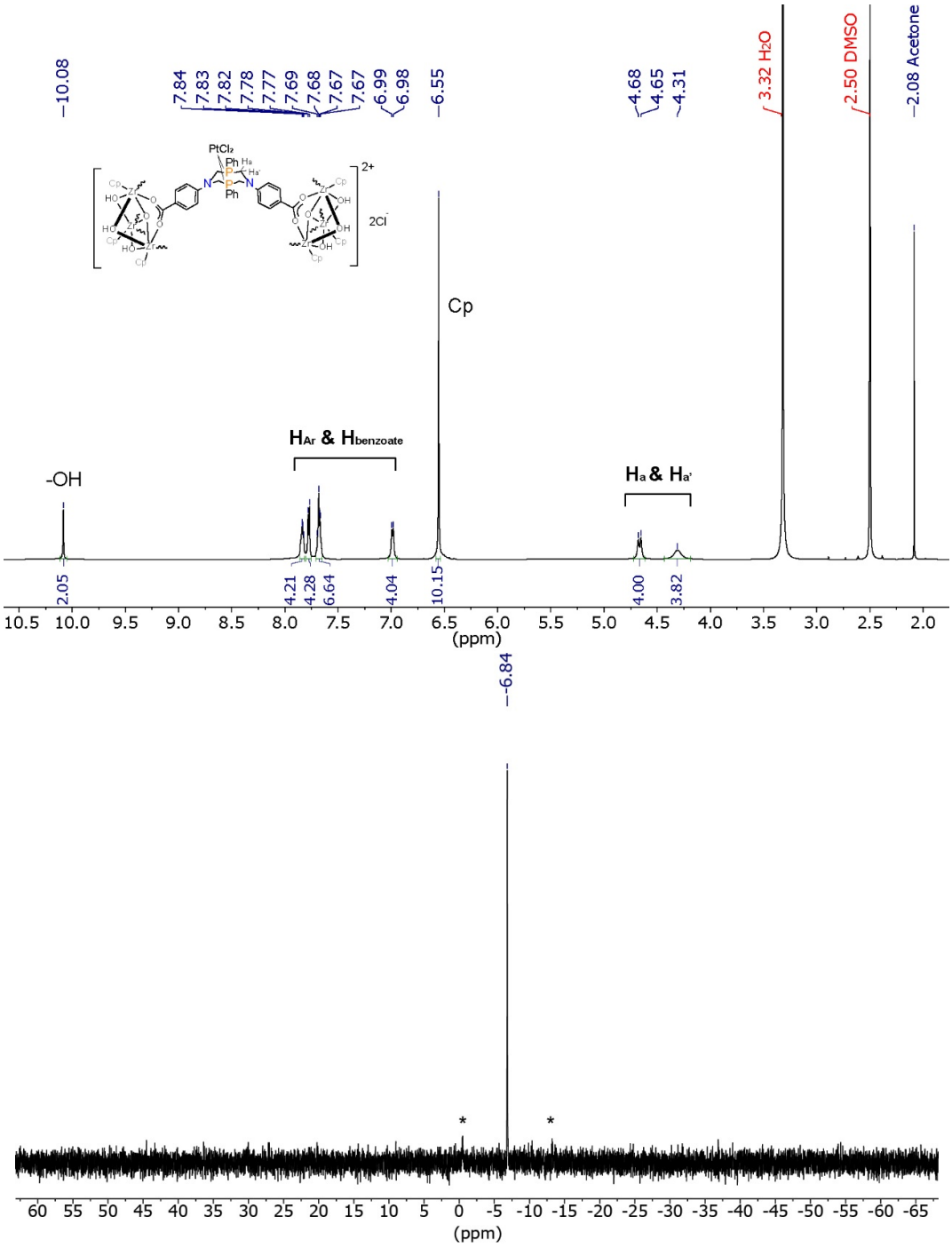

Figure S14. ^{1}H and ^{31}P{^{1}H} NMR spectra of **Zr-P$_2$N$_2$-PtCl$_2$** from direct synthesis.

(DMSO-d_6, 600 MHz and 243 MHz).
The * symbol in the ^{31}P NMR spectra denotes "satellites" that result from ^{195}Pt-^{31}P coupling.

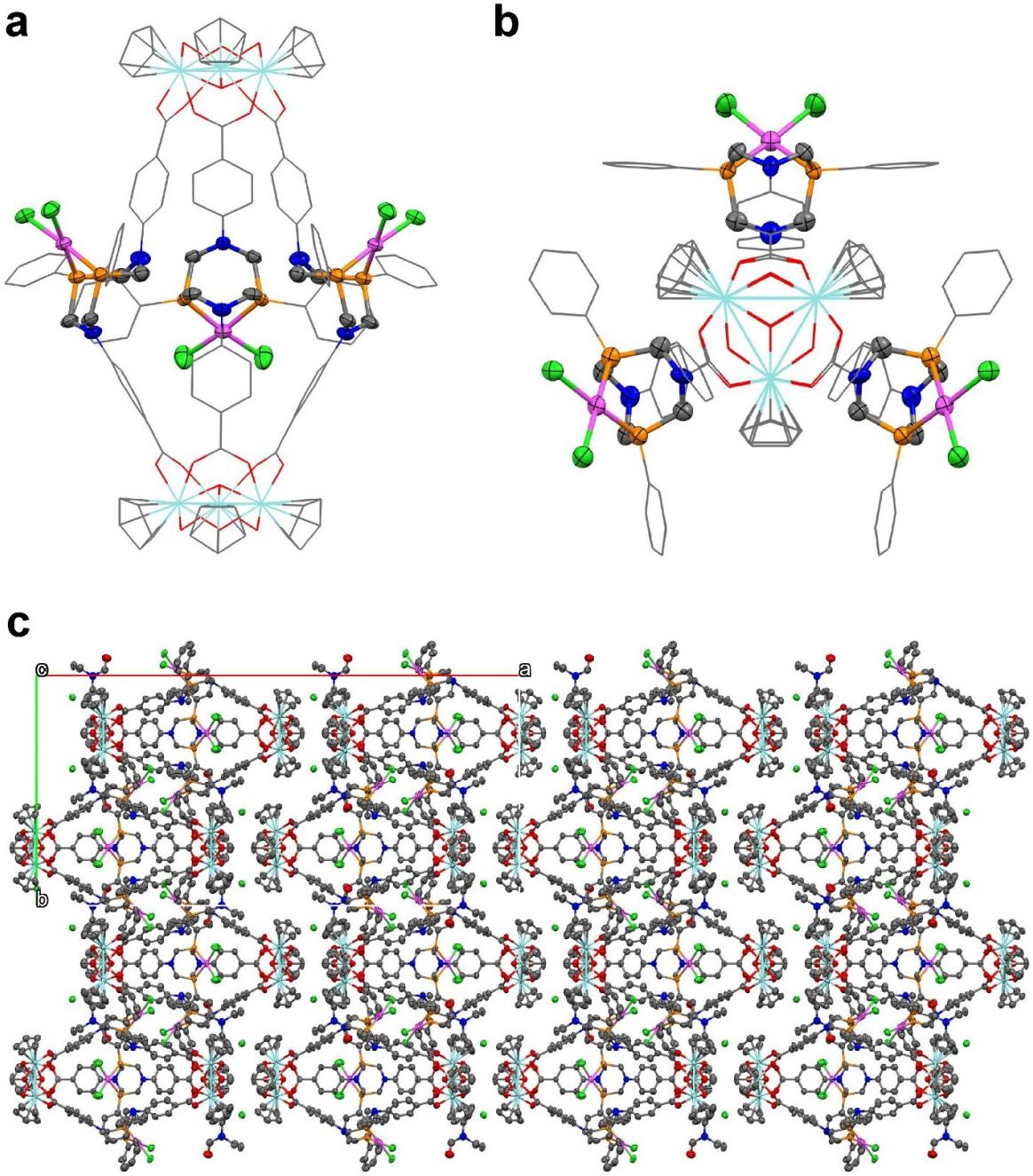

Figure S15. (a), (b) Structure of **Zr-P_2N_2-$PdCl_2$** (c) Packing of **Zr-P_2N_2-$PdCl_2$** viewed along the *c*-axis.

(Cyan: Zr, red: O, blue: N, orange: P, gray: C, green: Cl, magenta: Pd) Hydrogen atoms are omitted for clarity.

Table S3. Crystal data and structure refinement for **Zr-P_2N_2-$PdCl_2$**.

Empirical formula	$C_{180}H_{240}Cl_8N_{18}O_{32}P_6Pd_3Zr_6$
Formula weight	4503.83
Temperature/K	100
Crystal system	orthorhombic
Space group	Pnma
a/Å	47.908(4)
b/Å	22.924(2)
c/Å	17.5652(18)
α/°	90
β/°	90
γ/°	90
Volume/Å^3	19291(3)
Z	4
ρ_{calc}g/cm^3	1.551
μ/mm^{-1}	0.817
F(000)	9224.0
Crystal size/mm^3	0.8 × 0.7 × 0.5
Radiation	MoKα (λ = 0.71073)
2Θ range for data collection/°	3.836 to 49.646
Index ranges	-56 ≤ h ≤ 56, -27 ≤ k ≤ 27, -20 ≤ l ≤ 20
Reflections collected	364785
Independent reflections	17009 [R_{int} = 0.0760, R_{sigma} = 0.0305]
Data/restraints/parameters	17009/975/852
Goodness-of-fit on F^2	1.111
Final R indexes [I>=2σ (I)]	R_1 = 0.1044, wR_2 = 0.2440
Final R indexes [all data]	R_1 = 0.1431, wR_2 = 0.2810
Largest diff. peak/hole / e Å^{-3}	2.41/-1.27

A solvent mask was calculated, and 1839 electrons were found in a volume of 7592 Å^3 in 1 void per unit cell. This is consistent with the presence of 32[$C_5H_{11}NO$ (DEF)], which accounts for 1792 electrons per unit cell. Due to significant solvent disorder, we were unable to precisely determine the solvent occupancy within the cavities via direct refinement. However, the solvent content was estimated by modeling the residual electron density (Q peaks) as DEF molecules with free chemical occupancy and applying the SQUEEZE procedure to the interstitial Q peaks. Using this method, 1848 electrons (6794 Å^3 in 3 voids) were identified per unit cell. This is consistent with the presence of 32 DEF molecules (1792 electrons) per unit cell and indicates that there are no DEF molecules residing inside the cage cavities.

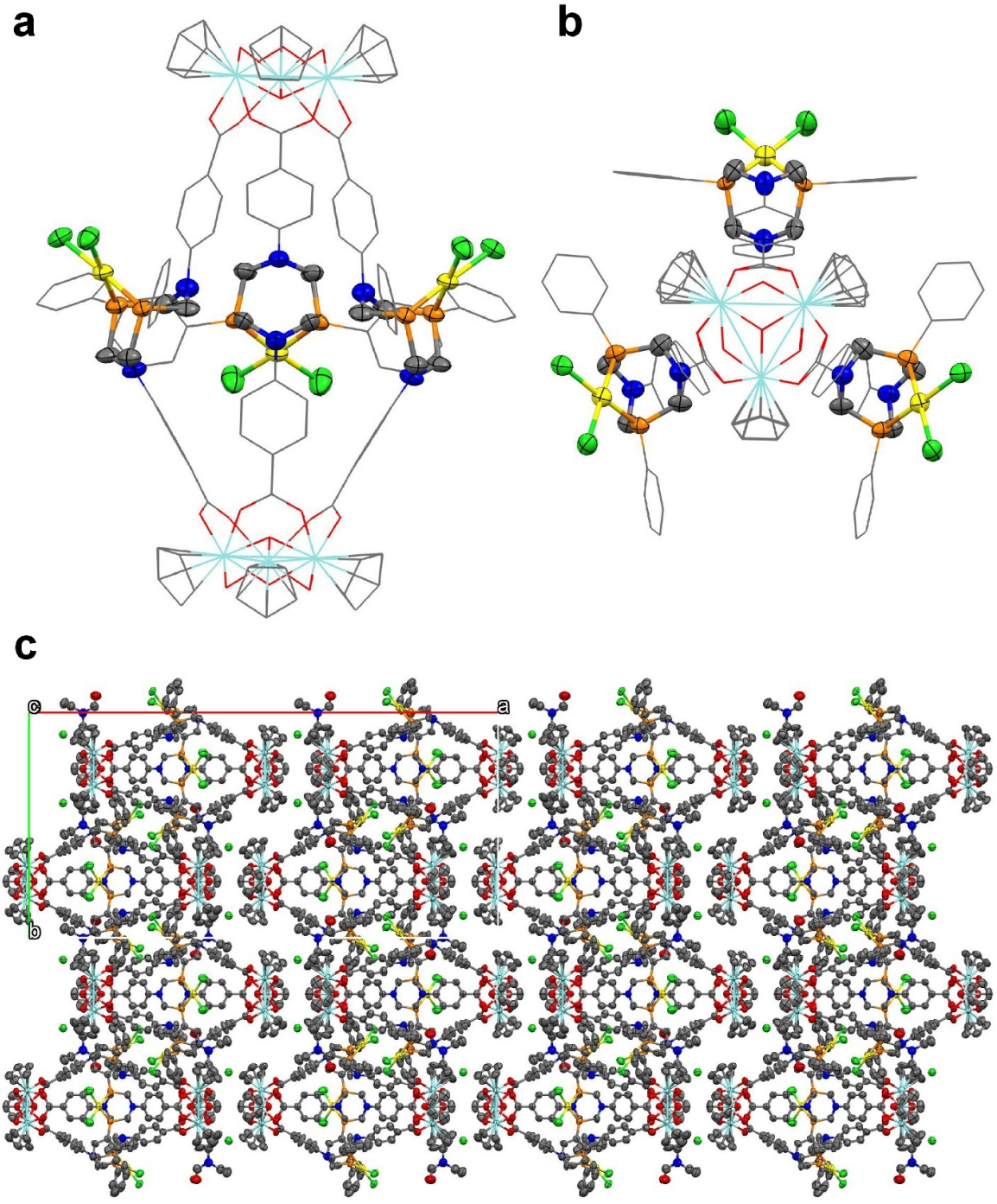

Figure S16. (a), (b) The structure of **Zr-P_2N_2-$PtCl_2$** (c) Packing of **Zr-P_2N_2-$PtCl_2$** viewed along the *c*-axis. (Cyan: Zr, red: O, blue: N, orange: P, gray: C, green: Cl, yellow: Pt) Hydrogen atoms are omitted for clarity.

Table S4. Crystal data and structure refinement for **Zr-P_2N_2-$PtCl_2$**.

Empirical formula	$C_{165}H_{207}Cl_8N_{15}O_{29}P_6Pt_3Zr_6$
Formula weight	3758.42
Temperature/K	240
Crystal system	orthorhombic
Space group	Pnma
a/Å	48.134(3)
b/Å	23.0579(18)
c/Å	17.7804(14)
α/°	90
β/°	90
γ/°	90
Volume/Å^3	19734(3)
Z	4
ρ_{calc}g/cm^3	1.265
μ/mm^{-1}	2.626
F(000)	7368.0
Crystal size/mm^3	0.28 × 0.19 × 0.13
Radiation	MoKα (λ = 0.71073)
2Θ range for data collection/°	3.818 to 49.756
Index ranges	$-56 \leq h \leq 56$, $-27 \leq k \leq 27$, $-20 \leq l \leq 21$
Reflections collected	548029
Independent reflections	17490 [R_{int} = 0.0604, R_{sigma} = 0.0204]
Data/restraints/parameters	17490/942/774
Goodness-of-fit on F^2	1.103
Final R indexes [I>=2σ (I)]	R_1 = 0.1032, wR_2 = 0.2170
Final R indexes [all data]	R_1 = 0.1334, wR_2 = 0.2408
Largest diff. peak/hole / e Å^{-3}	3.97/-1.92

A solvent mask was calculated, and 1596 electrons were found in a volume of 7878 Å^3 in 1 void per unit cell. This is consistent with the presence of 28 [$C_5H_{11}NO$ (DEF)], which accounts for 1568 electrons per unit cell.

Due to significant solvent disorder, we were unable to precisely determine the solvent occupancy within the cavities via direct refinement. However, we estimated the solvent content by modeling the residual electron density (Q peaks) as DEF molecules with free chemical occupancy and applying the SQUEEZE procedure to the interstitial Q peaks. Through this method, 1611 electrons (6828 Å^3 in 2 voids) were identified per unit cell. This is consistent with the presence of 28 DEF molecules (1568 electrons) per unit cell. This indicates that there is no DEF molecule that resides inside cage cavities.

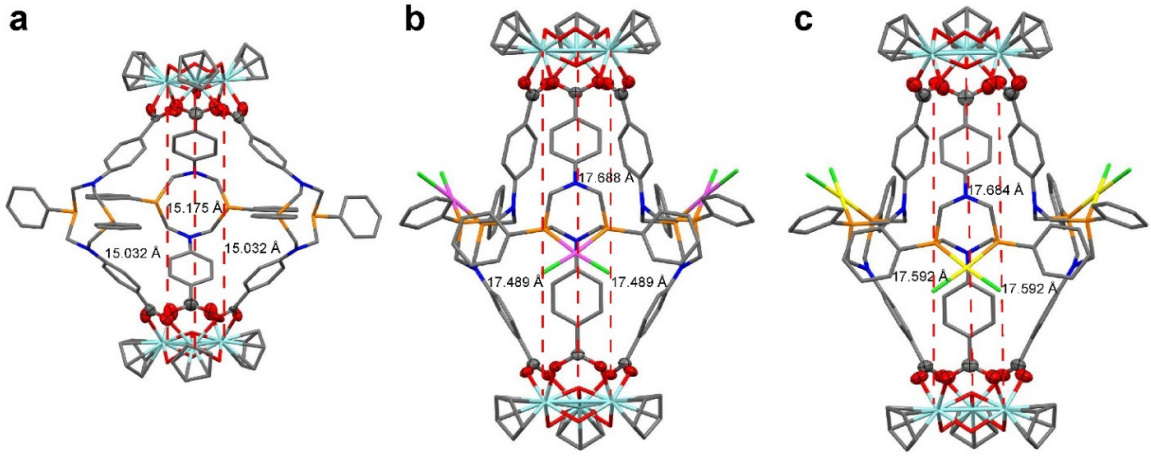

Figure S17. Distances between Zr metal nodes of (a) **Zr-P_2N_2**, (b) **Zr-P_2N_2-$PdCl_2$**, and (c) **Zr-P_2N_2-$PtCl_2$**.

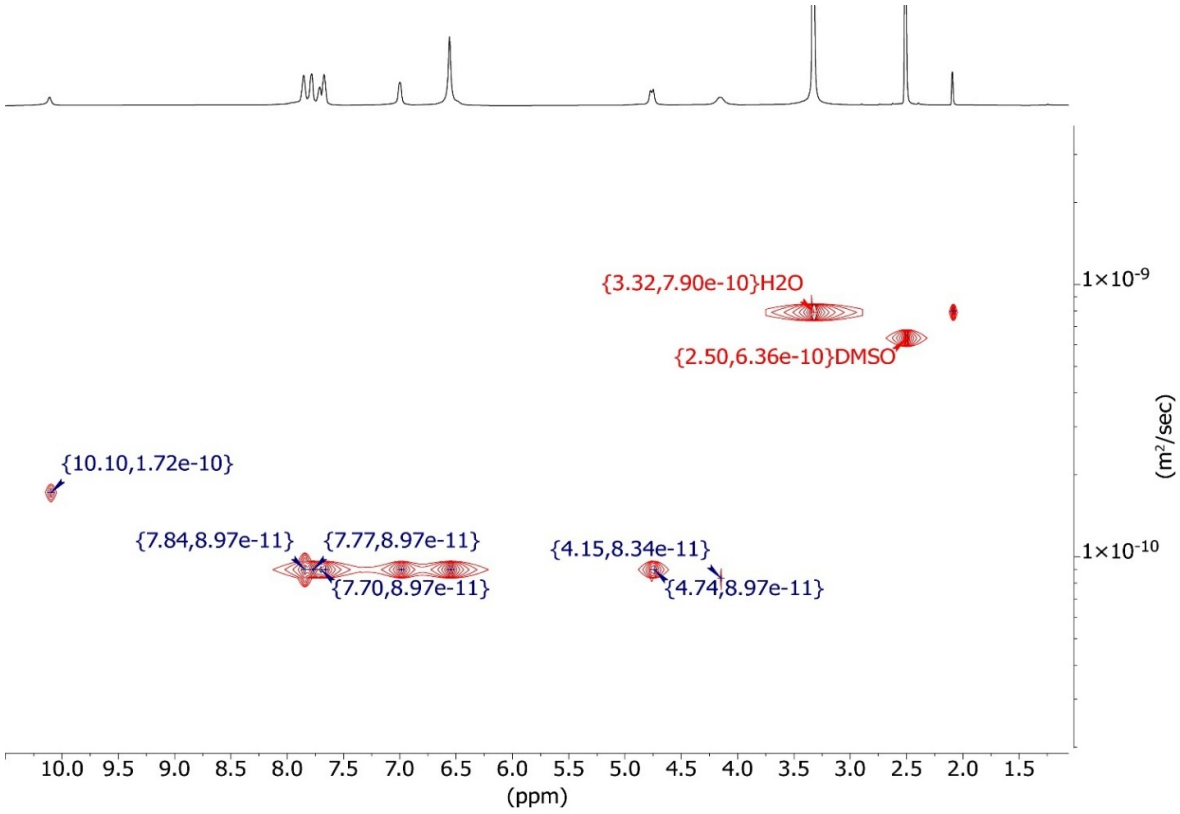

Figure S18. ^{1}H DOSY NMR spectrum of **Zr-P_2N_2-$PdCl_2$** MOC in DMSO-d_6.

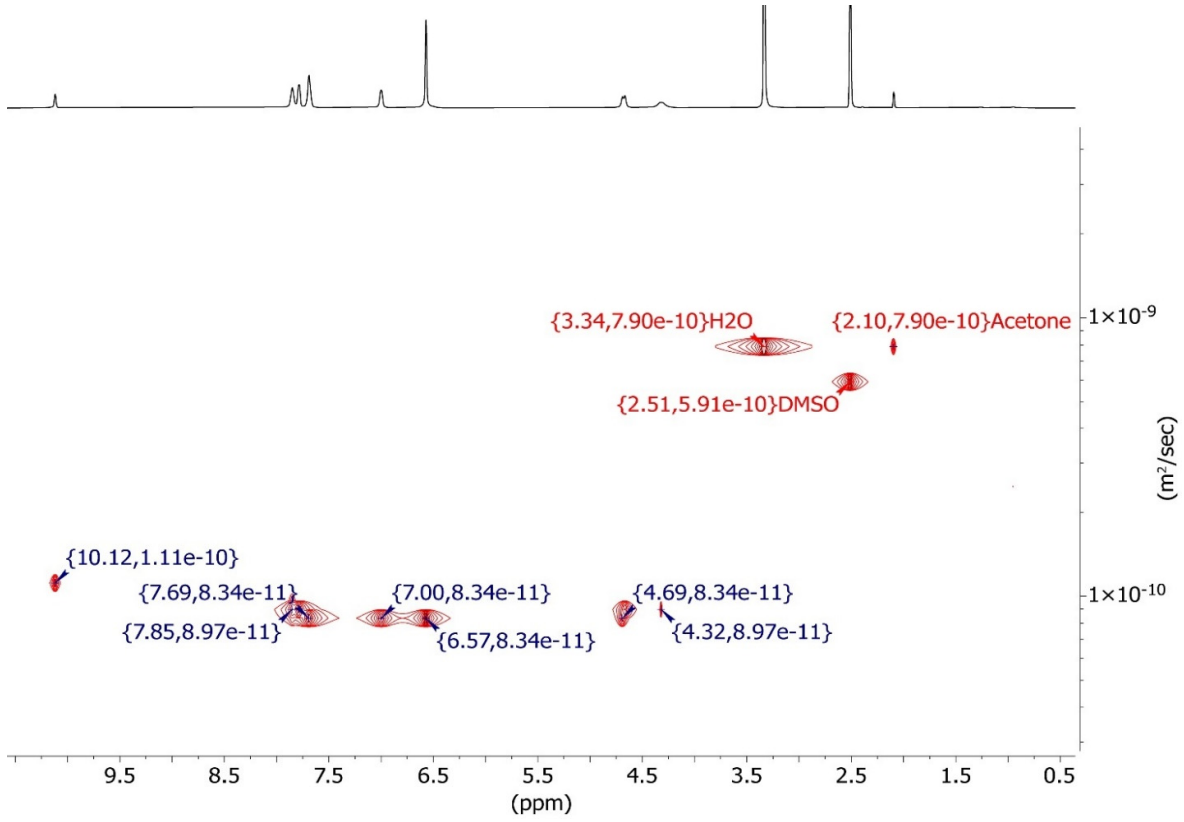

Figure S19. ^{1}H DOSY NMR spectrum of **Zr-P_2N_2-$PtCl_2$** MOC in DMSO-d_6.

Table S5. Average diffusion coefficients (D) and hydrodynamic radii of **Zr-P_2N_2** and **Zr-P_2N_2-MCl_2**.

MOC	Average diffusion coefficient (D) in DMSO-d_6	Hydrodynamic radii R_H (nm)
Zr-P_2N_2	7.98×10^{-11}	1.38
Zr-P_2N_2-$PdCl_2$	8.89×10^{-11}	1.24
Zr-P_2N_2-$PtCl_2$	8.61×10^{-11}	1.28

Hydrodyamic radii values were calculated using the Einstein-Stokes equation. [1]

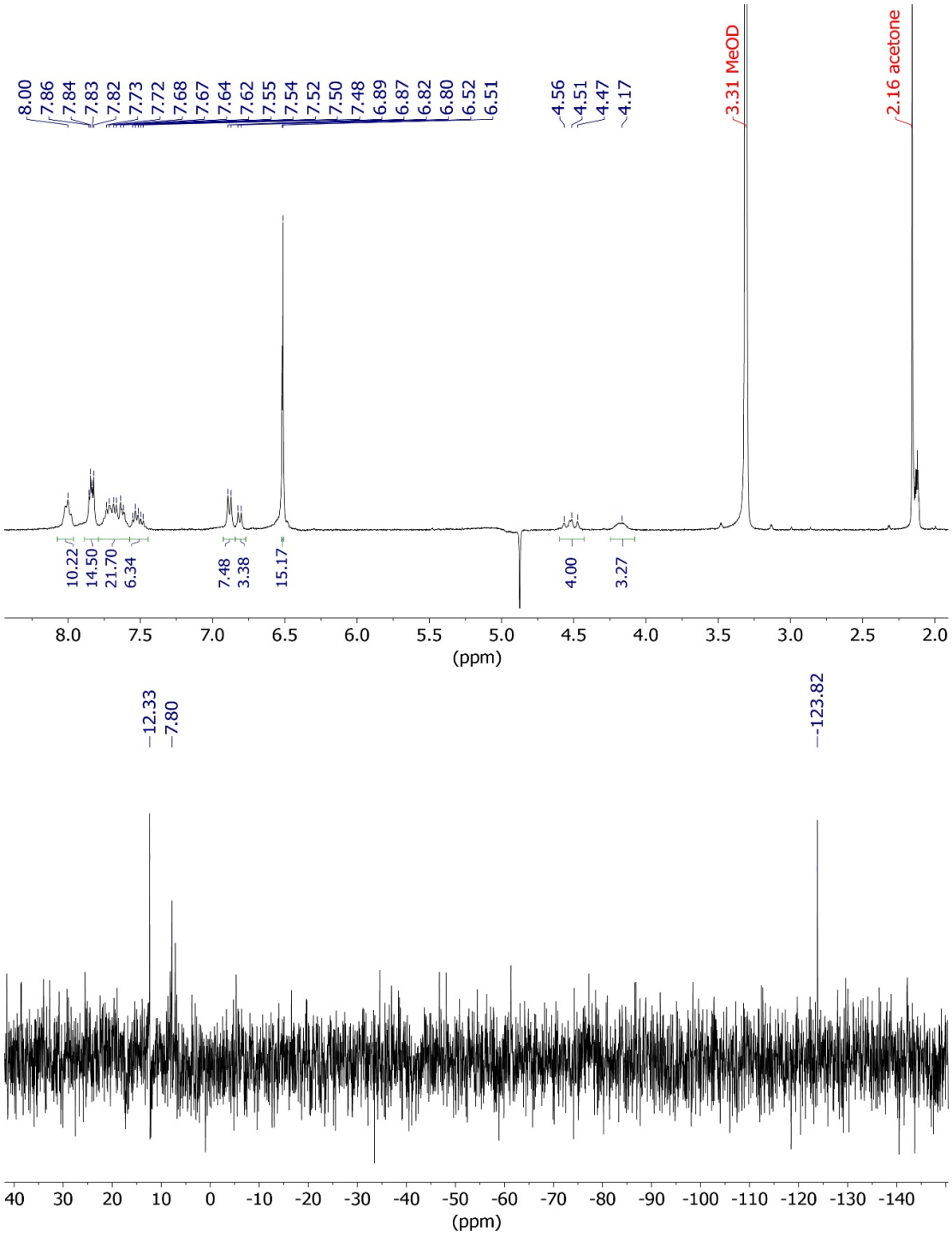

Figure S20. ^{1}H and $^{31}P\{^{1}H\}$ NMR spectra of **Zr-P_2N_2-$PdCl_2$** in methanol-d_4. (400 MHz and 162 MHz).

Water suppression was used in the ^{1}H NMR spectrum due to the poor solubility of the cage.

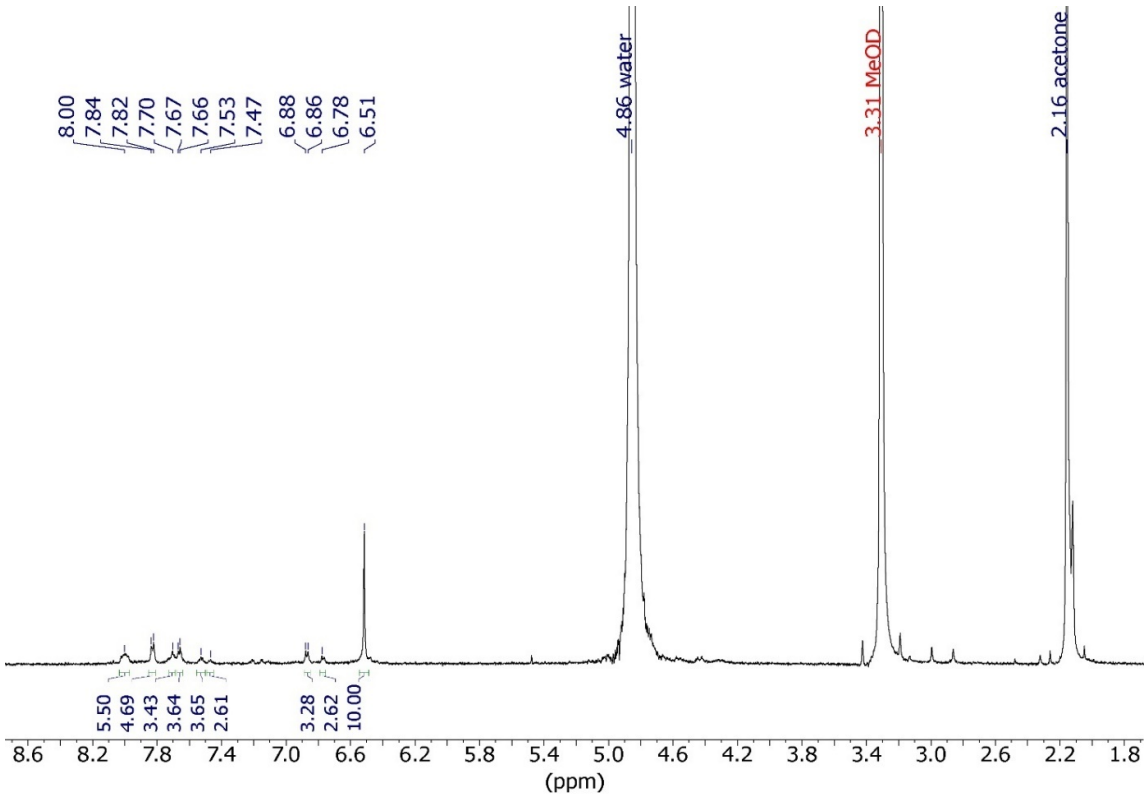

Figure S21. ^{1}H NMR spectrum of **Zr-P_2N_2-$PtCl_2$** in methanol-d_4.

(400 MHz and 162 MHz).

The ^{31}P NMR spectrum did not show a discernible resonance due to the poor solubility of the cage.

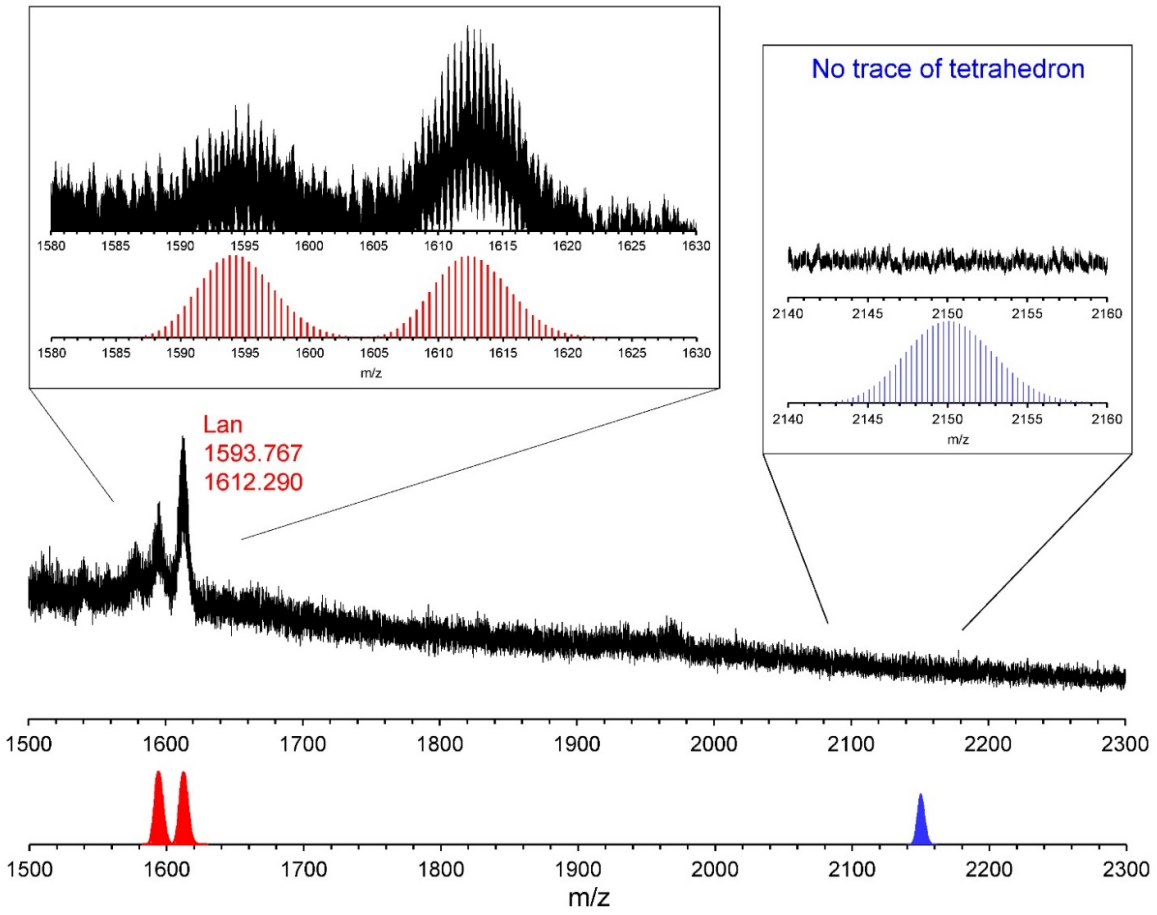

Assignments	m/z experimental	m/z simulated
Lantern $(C_{120}H_{114}Cl_6N_6O_{20}P_6Pd_3Zr_6)^{2+}$ $\{[(ZrCp)_3O(OH)_3]_2(P_2N_2\text{-}PdCl_2)_3\}^{2+}$	1612.290	1612.304
Lantern (-HCl) $(C_{120}H_{113}Cl_5N_6O_{20}P_6Pd_3Zr_6)^{2+}$	1593.767	1593.816

Figure S22. Simulated and experimental MALDI-TOF spectra of **Zr-P_2N_2-$PdCl_2$**.

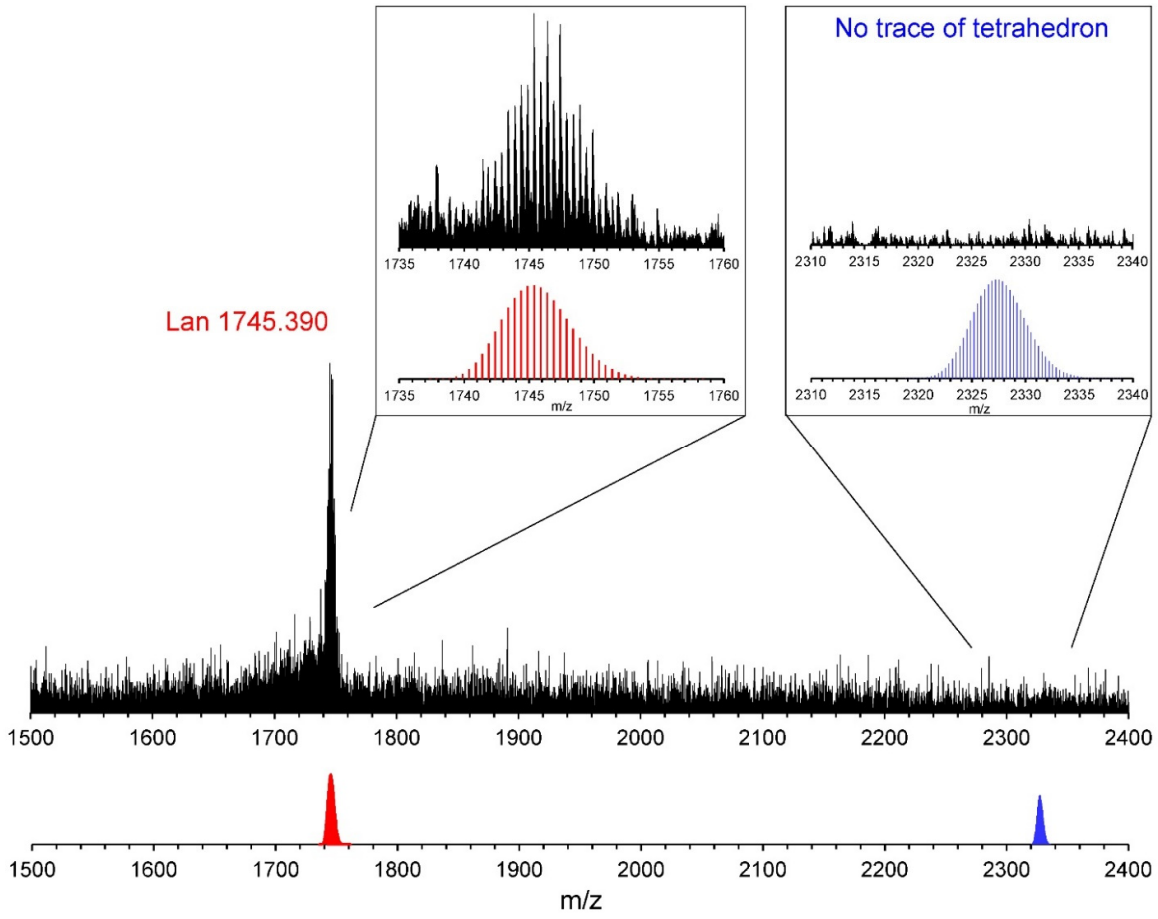

Assignments	m/z experimental	m/z simulated
Lantern $(C_{120}H_{114}Cl_6N_6O_{20}P_6Pt_3Zr_6)^{2+}$ $\{[(ZrCp)_3O(OH)_3]_2(P_2N_2\text{-}PtCl_2)_3\}^{2+}$	1745.390	1745.394

Figure S23. Simulated and experimental MALDI-TOF spectra of **Zr-P_2N_2-$PtCl_2$**.

Attempted PF_6^-/Cl^- salt metathesis of Zr-P_2N_2-$PdCl_2$ and Zr-P_2N_2-$PtCl_2$

The **Zr-P_2N_2-MCl_2** cages were subject to PF_6^-/Cl^- salt metathesis with $AgPF_6$ in an attempt to improve their solubility in aprotic solvents for ESI-MS and reactivity studies. **Zr-P_2N_2-$PdCl_2$** and **Zr-P_2N_2-$PtCl_2$** were treated with 2 equiv. of $AgPF_6$ in DMSO solution. After filtration to remove AgCl precipitate, the products, **Zr-P_2N_2-MPF_6** (M=Pd, Pt), were isolated by precipitation with ethyl acetate. ^{31}P NMR spectra in DMSO-d_6 show a single resonance at +10.5 and -6.6 ppm for **Zr-P_2N_2-$PdPF_6$** and **Zr-P_2N_2-$PtPF_6$**, respectively, consistent with the presence of symmetric species resembling the **Zr-P_2N_2-MCl_2** precursors (Figure S24-S25). The ^{1}H NMR spectra were also nearly indistinguishable from those of the parent cages. Together, these data support metathesis of the outer sphere, charge-balancing Cl^- ions rather than the MCl_2 moieties.

The **Zr-P_2N_2-MPF_6** products exhibit improved solubility in MeCN. However, NMR analysis in MeCN-d_3 revealed the formation of multiple new species, which are most apparent from the appearance of new ^{1}H NMR resonances around 8.3-8.5 ppm (Zr–OH) and in the 4-5 ppm (CH_2) region (Figure S26-S27). The chemical shift of the Zr–OH groups has been shown by Cook and co-workers to be diagnostic of lantern versus tetrahedral cage structures, with the Zr–OH groups of tetrahedral cages appearing slightly more downfield.[2] Indeed, the ESI-MS data for **Zr-P_2N_2-$PdPF_6$** and **Zr-P_2N_2-$PtPF_6$** in MeCN solution show a series of new mass signals associated with a mixture of lantern, tetrahedron, and perhaps even cubic-type structures (Figure S28-S29). The dominant signals for the parent cages (z = +2, 1583.91 amu for Pd, 1716.99 amu for Pt) clearly overlap with a second mass signal exhibiting an isotopic distribution expected for a tetrahedral cage (z = +4). This is further corroborated by the appearance of a z = +3 mass signal (2112.21 amu for Pd and 2289.33 amu for Pt) which can only arise from the presence of tetrahedral cages. The data also indicate the loss of 2 Cl^- ions from the core structure and the addition of a OH^- group. Altogether, the NMR and ESI-MS data indicate that **Zr-P_2N_2-$PdPF_6$** and **Zr-P_2N_2-$PtPF_6$** undergo structural rearrangement in MeCN solution.

Solvent-dependent structural rearrangements in coordination cages have been reported.[3,4] For example, Yoshizawa and coworkers described solvent-driven interconversions between a peanut-shaped M_2L_4 capsule and a ML_2 double tube structure upon when switching between DMSO and CD_3CN/D_2O solvents.[5] They proposed that the double tube represents an entropically favored product in the more polar DMSO solvent. In the present case, a mixture of species is observed by NMR and ESI-MS, and we have been unable to isolate the new species, limiting further investigation of the structural rearrangement.

Procedures for PF_6^-/Cl^- salt metathesis of Zr-P_2N_2-$PdCl_2$ and Zr-P_2N_2-$PtCl_2$

A 0.1 M $AgPF_6$ solution was prepared in DMSO (2 mL). **Zr-P_2N_2-$PdCl_2$** (20 mg, 0.006 mmol) and **Zr-P_2N_2-$PtCl_2$** (28 mg, 0.008 mmol) were suspended in DMSO (5 mL), respectively, and 2 equiv. of $AgPF_6$ was added to each suspension. The mixture was stirred overnight at room temperature. The resulting white solid (AgCl) was removed by filtration. Ethyl acetate (60 mL) was added to the filtrate, resulting in precipitation of the Zr-P_2N_2-MPF_6 products. The yellow (Pd) and white (Pt) precipitates were isolated by filtration, washed with ethyl acetate, and dried in vacuo.

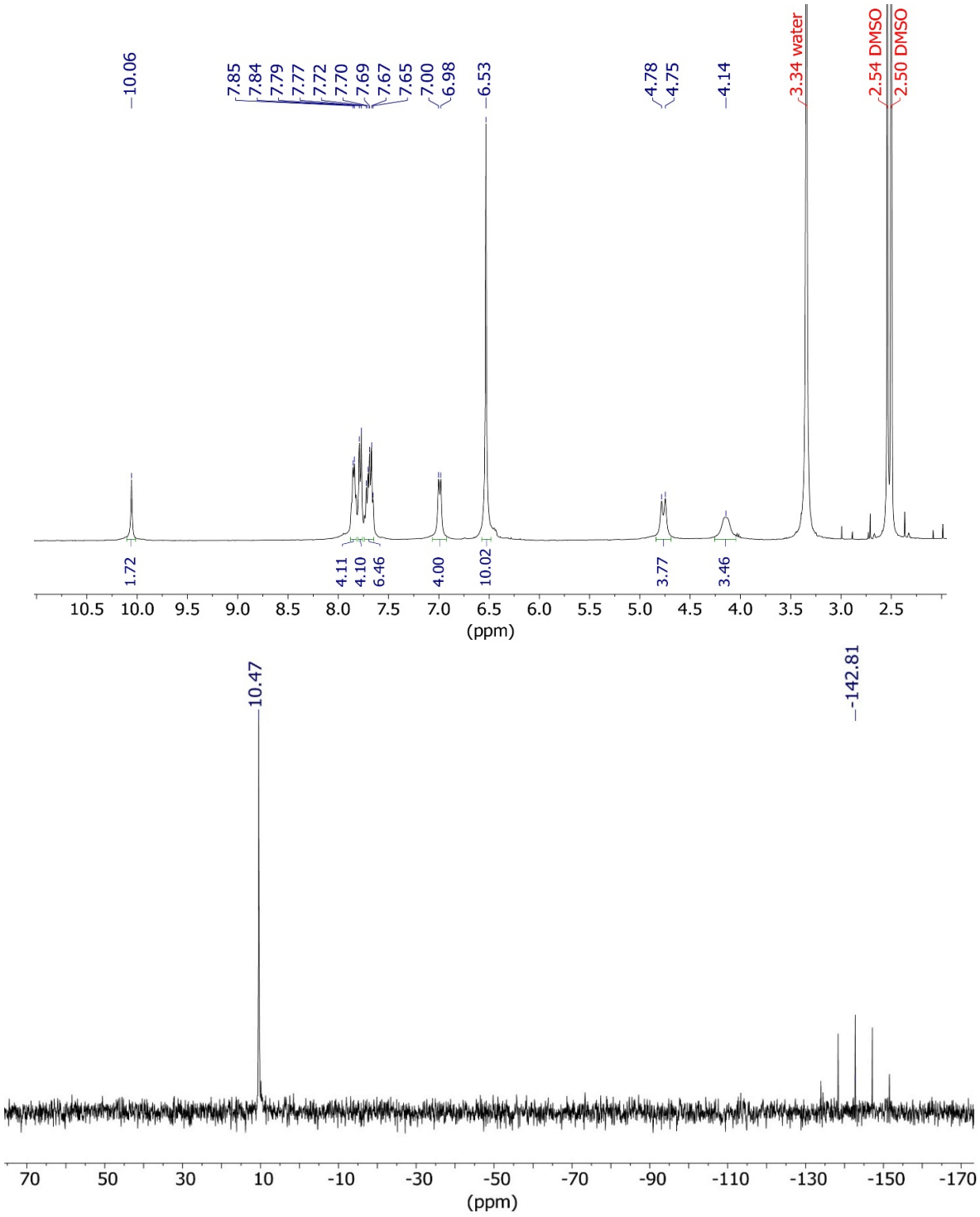

Figure S24. ^{1}H and $^{31}P\{^{1}H\}$ NMR spectra of **Zr-P_2N_2-PdPF$_6$** in DMSO-d_6. (400 MHz and 162 MHz).

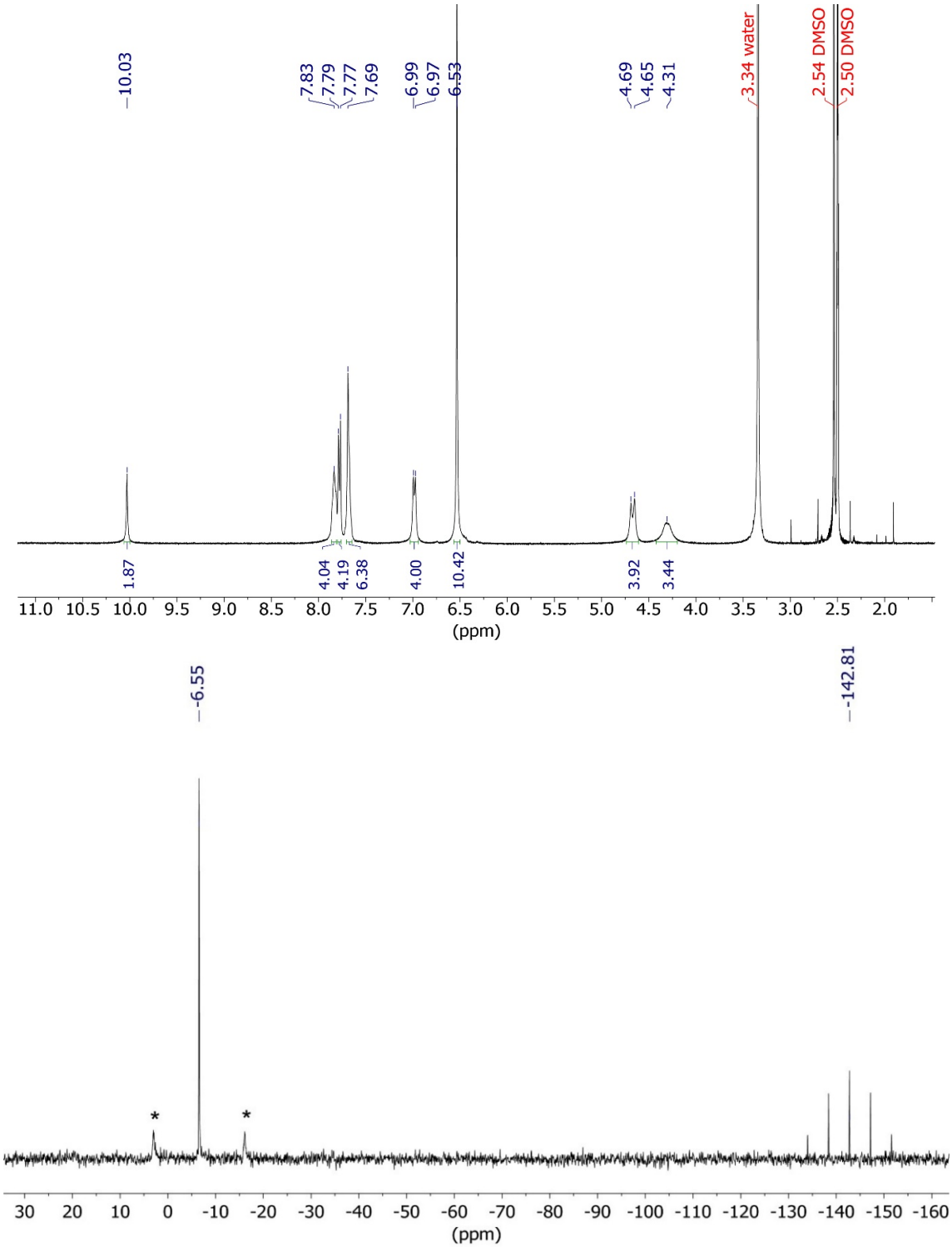

Figure S25. ^{1}H and $^{31}P\{^{1}H\}$ NMR spectra of **Zr-P_2N_2-PtPF$_6$** in DMSO-d_6. (400 MHz and 162 MHz).

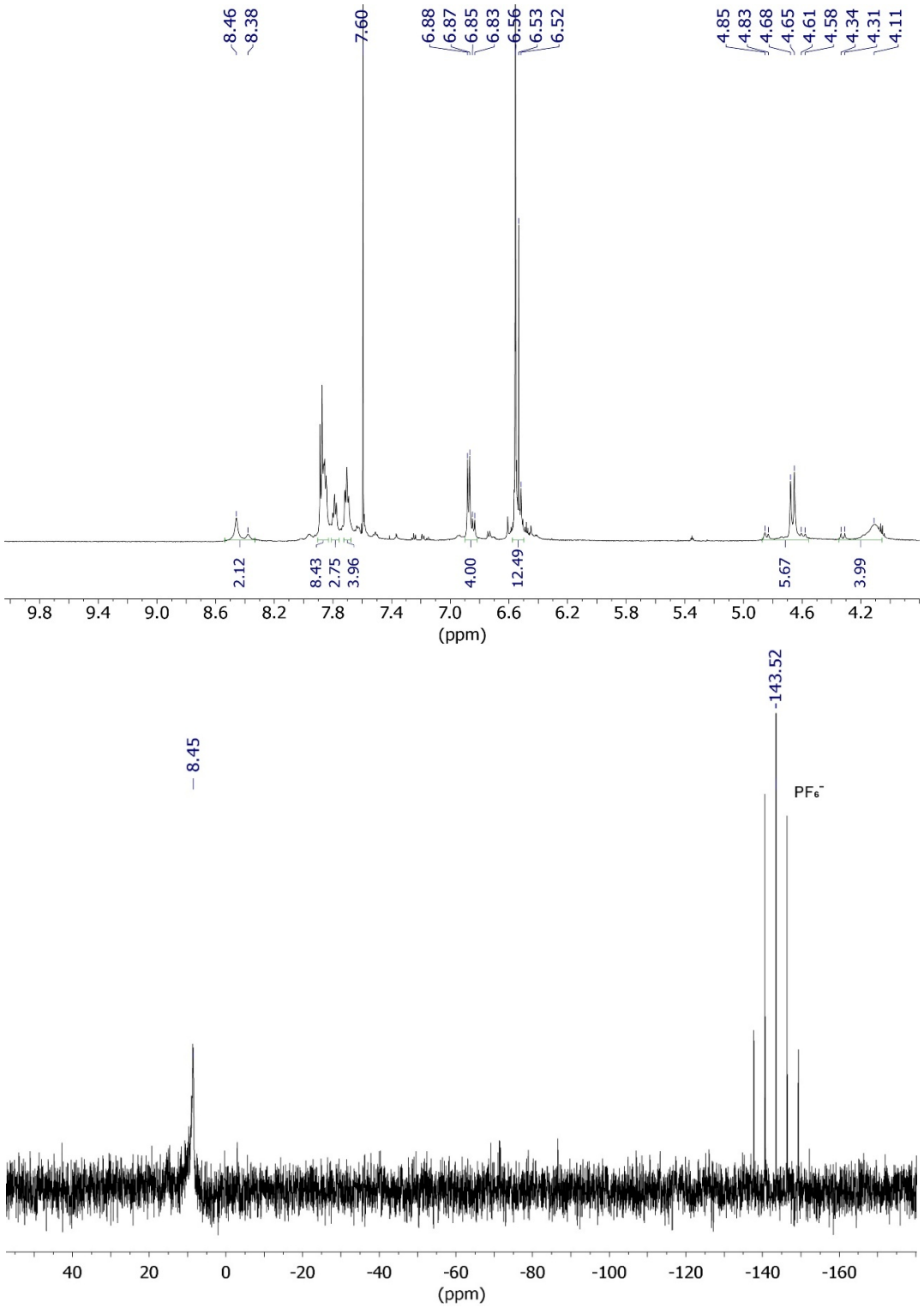

Figure S26. ^{1}H and $^{31}P\{^{1}H\}$ NMR spectra of **Zr-P_2N_2-PdPF_6** in CD_3CN. (600 MHz and 243 MHz).

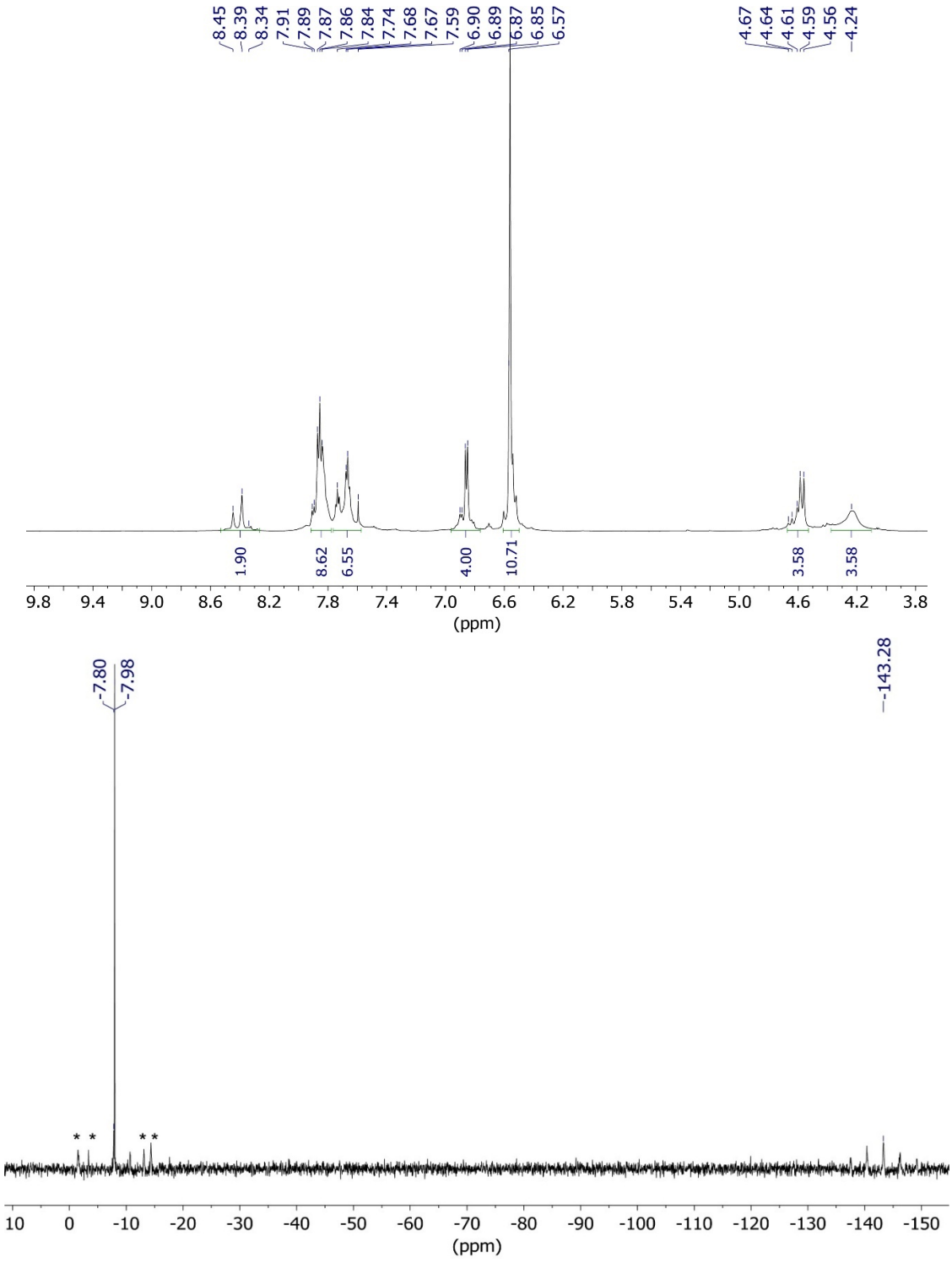

Figure S27. ^{1}H and $^{31}P\{^{1}H\}$ NMR spectra of **Zr-P_2N_2-PtPF$_6$** in CD_3CN.
(600 MHz and 243 MHz).

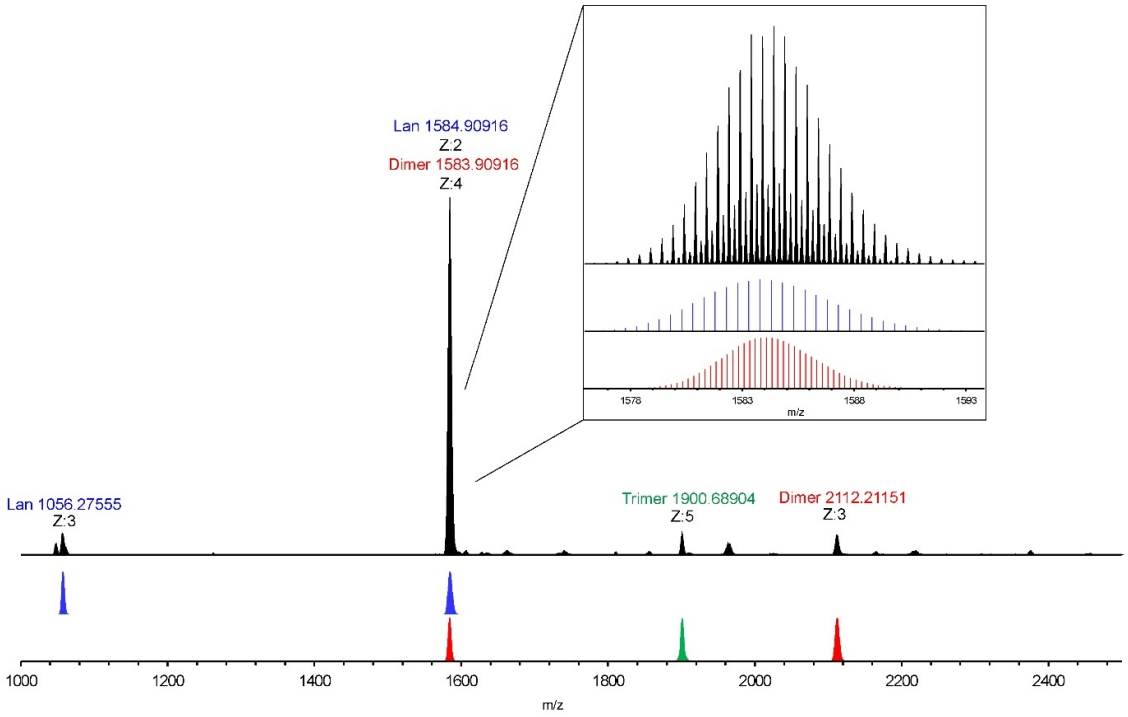

Assignments	m/z experimental	m/z simulated
Lantern $(C_{120}H_{112}Cl_4N_6O_{21}P_6Pd_3Zr_6)^{2+}$ $\{[(ZrCp)_3(O)_2(OH)_2][(ZrCp)_3(O)_3(OH)](P_2N_2\text{-}PdCl_2)_2(P_2N_2\text{-}PdOH)\}^{2+}$	1583.90916	1583.82517
Lantern $(C_{120}H_{113}Cl_4N_6O_{21}P_6Pd_3Zr_6)^{3+}$	1056.27555	1056.21921
Dimer (tetrahedron) $(C_{240}H_{223}Cl_8N_{12}O_{42}P_{12}Pd_6Zr_{12})^{3+}$	2112.21151	2112.10058
Dimer (tetrahedron) $(C_{240}H_{224}Cl_8N_{12}O_{42}P_{12}Pd_6Zr_{12})^{4+}$	1583.90916	1584.07530
Trimer $(C_{360}H_{335}Cl_{12}N_{18}O_{63}P_{18}Pd_9Zr_{18})^{5+}$	1900.68904	1900.78894

Sample was dissolved in acetonitrile and measured in positive mode with m/z from 200 to 3000.

Figure S28. Simulated and experimental ESI-MS spectra of **Zr-P_2N_2-PdPF$_6$**.

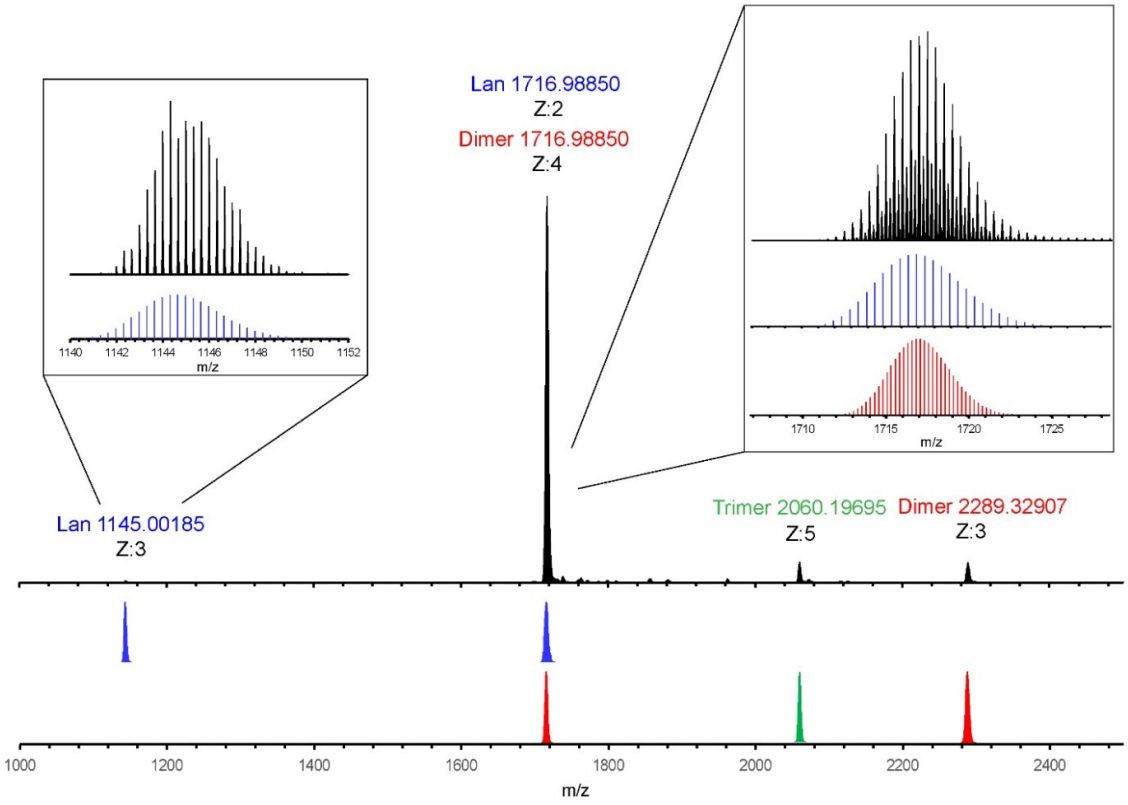

Sample was dissolved in acetonitrile and measured in positive mode with m/z from 200 to 3000.

Assignments	m/z experimental	m/z simulated
Lantern $(C_{120}H_{112}Cl_4N_6O_{21}P_6Pt_3Zr_6)^{2+}$ $\{[(ZrCp)_3(O)_2(OH)_2][(ZrCp)_3(O)_3(OH)](P_2N_2\text{-}PtCl_2)_2(P_2N_2\text{-}PtOH)\}^{2+}$	1716.98850	1716.91537
Lantern $(C_{120}H_{113}Cl_4N_6O_{21}P_6Pt_3Zr_6)^{3+}$	1145.00185	1144.94601
Dimer (tetrahedron) $(C_{240}H_{223}Cl_8N_{12}O_{42}P_{12}Pt_6Zr_{12})^{3+}$	2289.32907	2288.88475
Dimer (tetrahedron) $(C_{240}H_{224}Cl_8N_{12}O_{42}P_{12}Pt_6Zr_{12})^{4+}$	1716.98850	1716.91538
Trimer $(C_{360}H_{335}Cl_{12}N_{18}O_{63}P_{18}Pt_9Zr_{18})^{5+}$	2060.19695	2060.29710

Figure S29. Simulated and experimental ESI-MS spectra of **Zr-P_2N_2-$PtPF_6$**.

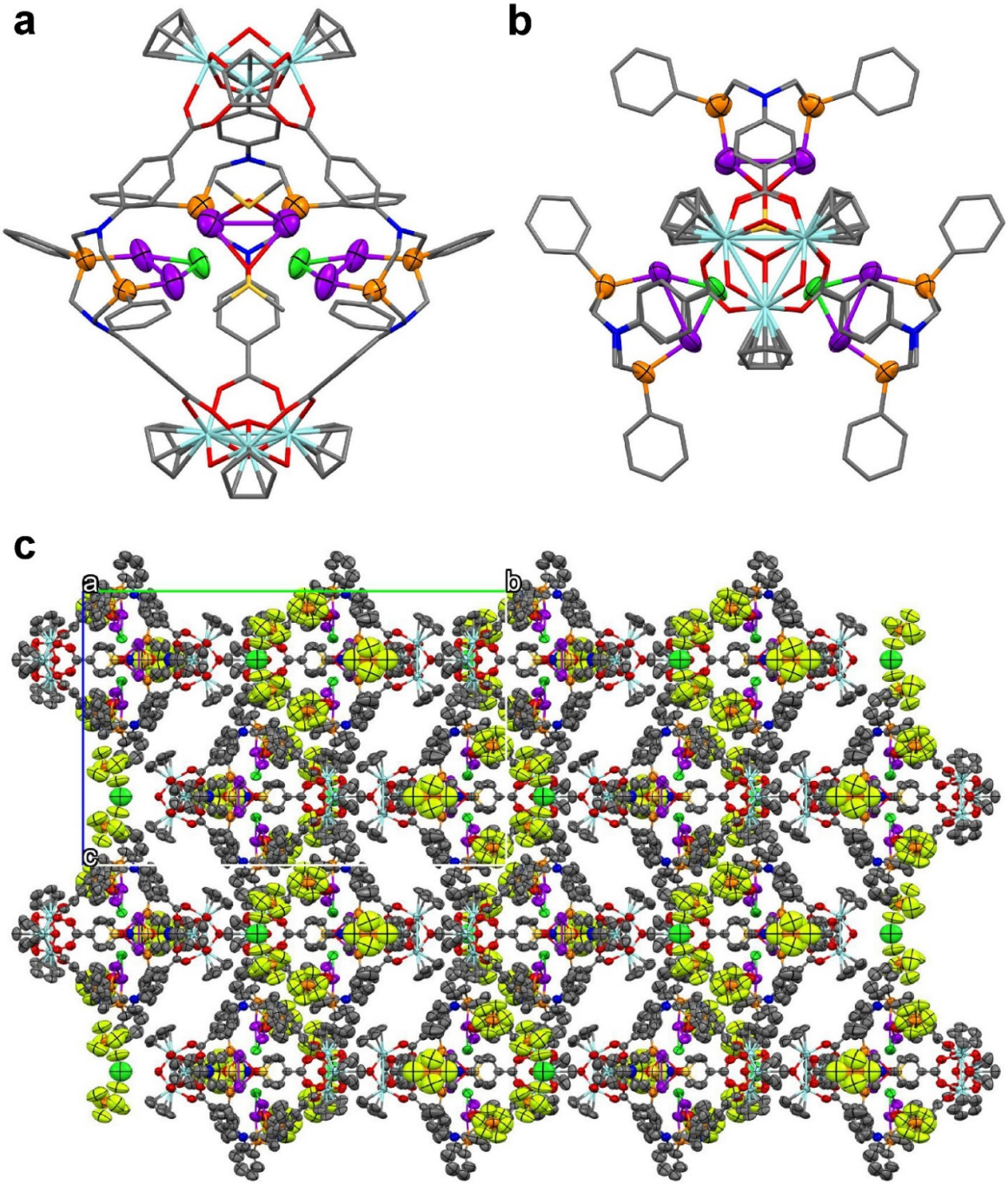

Figure S30. (a), (b) The structure of **Zr-P_2N_2-Ag** (c) Packing of **Zr-P_2N_2-Ag** viewed along the *a*-axis.

(Cyan: Zr, red: O, blue: N, orange: P, gray: C, green: Cl, purple: Ag, neon green: F, yellow: S) Hydrogen atoms are omitted for clarity.

Details of X-ray structure solution and refinement for Zr-P_2N_2-Ag

The structure solution and refinement of **Zr-P_2N_2-Ag** was limited by weak diffraction and significant disorder of solvent molecules and counteranions as well as the potential desolvation of the crystals. Despite several crystallization attempts using various solvent mixtures, the majority of crystals were either polycrystalline or weakly diffracting. Consequently, we report the highest-quality dataset obtained. Efforts to model all expected counteranions and achieve full charge balance by were hindered by disorder. Based on the core structure, six PF_6^- anions are anticipated per cage. However, only five could be modeled using strong restraints. A remaining site of high residual electron density (Q peak) was assigned as a Cl^- ion, as the refinement of an additional PF_6^- at this position was unsuccessful. Due to these challenges, the counteranions were also masked by using the SQUEEZE procedure. We present data for both solvent-masked and counteranion and solvent-masked sets. We recognize the limitations of the crystallographic data for **Zr-P_2N_2-Ag** and it is presented to provide structural connectivity and cage topology. The crystallographic results have been further validated using NMR spectroscopy and mass spectrometry.

Table S6. Crystal data and structure refinement for **Zr-P_2N_2-Ag** with interstitial solvents masked using SQUEEZE.

Empirical formula	$C_{190}H_{326}Ag_6Cl_3F_{30}N_6O_{55}P_{11}S_{35}Zr_6$
Formula weight	6908.21
Temperature/K	100
Crystal system	orthorhombic
Space group	*Pbcm*
a/Å	21.0912(14)
b/Å	40.752(3)
c/Å	26.4875(19)
α/°	90
β/°	90
γ/°	90
Volume/Å^3	22766(3)
Z	4
ρ_{calc}g/cm^3	2.016
μ/mm^{-1}	1.307
F(000)	14064.0
Crystal size/mm^3	0.02 × 0.01 × 0.01
Radiation	MoKα (λ = 0.71073)
2Θ range for data collection/°	3.668 to 45
Index ranges	$-22 \leq h \leq 22$, $-43 \leq k \leq 43$, $-28 \leq l \leq 28$
Reflections collected	303316
Independent reflections	15181 [R_{int} = 0.0665, R_{sigma} = 0.0252]
Data/restraints/parameters	15181/1222/952
Goodness-of-fit on F^2	2.674
Final R indexes [I>=2σ (I)]	R_1 = 0.1708, wR_2 = 0.5112
Final R indexes [all data]	R_1 = 0.2131, wR_2 = 0.5733
Largest diff. peak/hole / e Å^{-3}	3.21/-1.70

A mask including solvent molecules and counteranions was calculated, and 5297 electrons were found in a volume of 8900 Å^3 in 1 void per unit cell. This is consistent with the presence of 124 C_2H_6SO (DMSO) molecules, which account for 5208 electrons per unit cell.

Table S7. Crystal data and structure refinement for **Zr-P_2N_2-Ag** with both interstitial solvents and counteranions masked using SQUEEZE.

Empirical formula	$C_{188}H_{317}Ag_6Cl_2F_{36}N_6O_{54}P_{12}S_{34}Zr_6$
Formula weight	6936.58
Temperature/K	100
Crystal system	orthorhombic
Space group	*Pbcm*
a/Å	21.0912(14)
b/Å	40.752(3)
c/Å	26.4875(19)
α/°	90
β/°	90
γ/°	90
Volume/Å^3	22766(3)
Z	4
ρ_{calc}g/cm^3	2.024
μ/mm^{-1}	1.297
F(000)	14092.0
Crystal size/mm^3	0.02 × 0.01 × 0.01
Radiation	MoKα (λ = 0.71073)
2Θ range for data collection/°	3.668 to 46.698
Index ranges	-22 ≤ h ≤ 23, -45 ≤ k ≤ 45, -29 ≤ l ≤ 29
Reflections collected	321070
Independent reflections	16843 [R_{int} = 0.0695, R_{sigma} = 0.0280]
Data/restraints/parameters	16843/962/738
Goodness-of-fit on F^2	2.238
Final R indexes [I>=2σ (I)]	R_1 = 0.1501, wR_2 = 0.4673
Final R indexes [all data]	R_1 = 0.1942, wR_2 = 0.5190
Largest diff. peak/hole / e Å^{-3}	1.65/-1.62

A mask including solvent molecules and counteranions was calculated and 6953 electrons were found in a volume of 12286 Å^3 in 1 void per unit cell. This is consistent with the presence of 128 C_2H_6SO (DMSO), 24 PF_6^-, which account for 7032 electrons per unit cell.

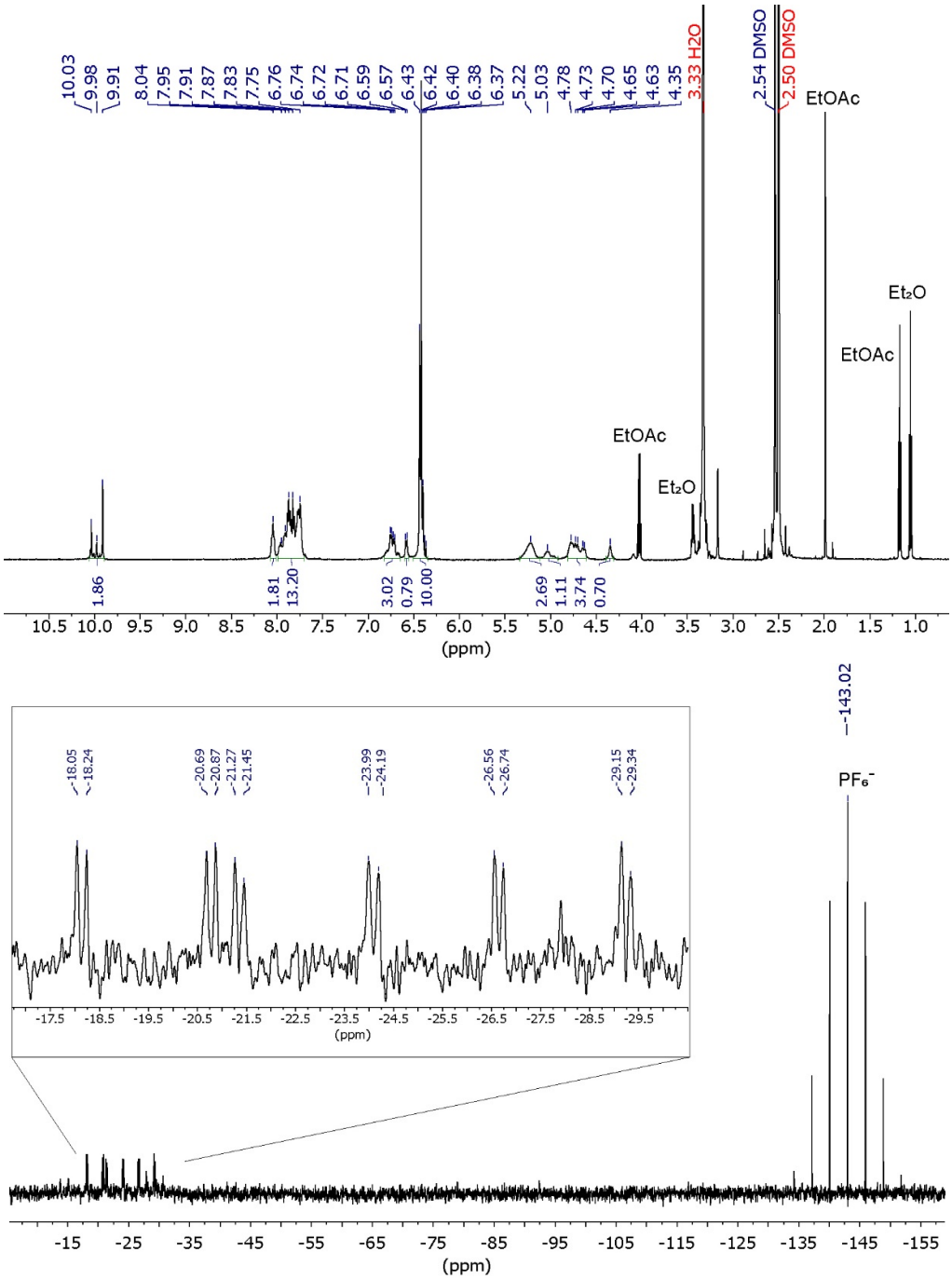

Figure S31. ^{1}H and ^{31}P{^{1}H} NMR spectra of crystalline **Zr-P$_2$N$_2$-Ag** in DMSO-d_6.

(600 MHz and 243 MHz)

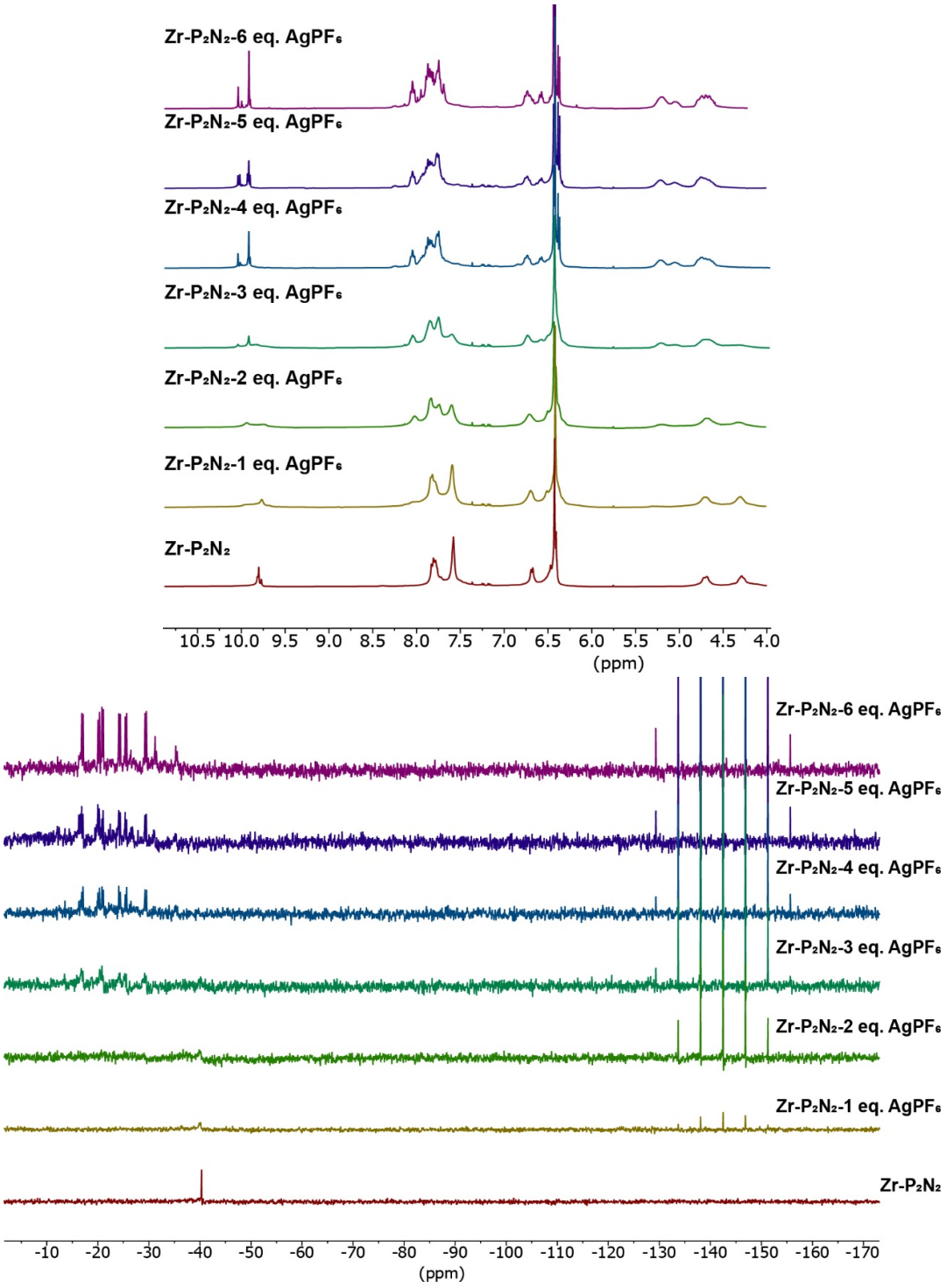

Figure S32. ^{1}H and $^{31}P\{^{1}H\}$ NMR spectra for titration of **Zr-P_2N_2** with $AgPF_6$ in DMSO-d_6.

(400 MHz and 162 MHz)

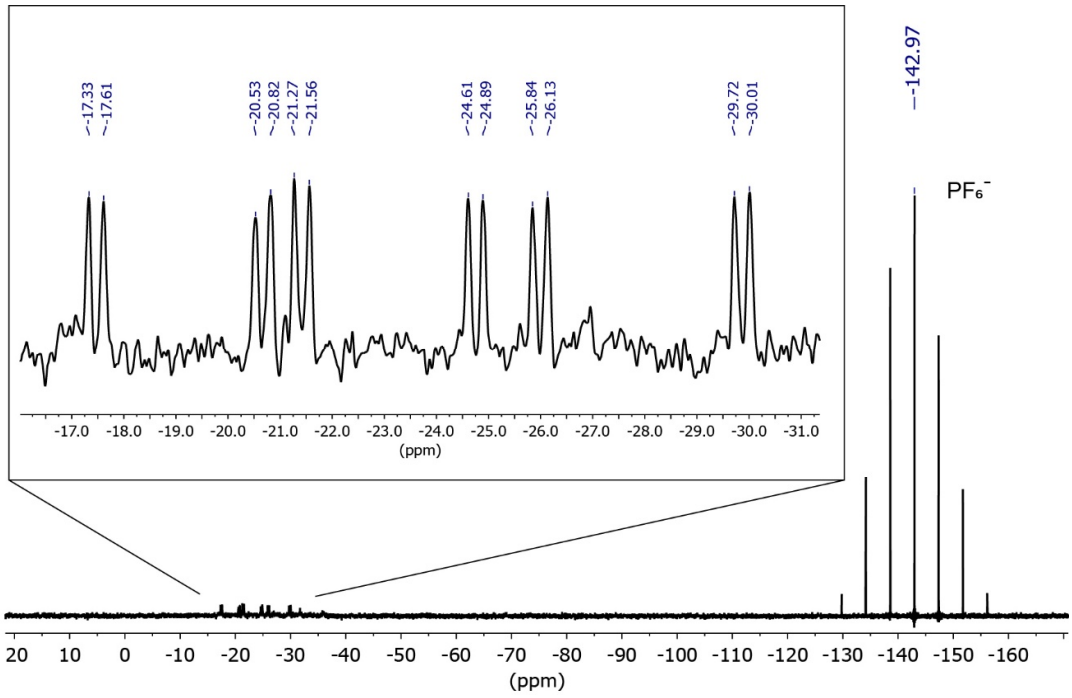

Figure S33. $^{31}P\{^{1}H\}$ NMR spectrum of **Zr-P_2N_2-Ag** by titration of **Zr-P_2N_2** with $AgPF_6$ (6 equiv) in DMSO-d_6.

(162 MHz)

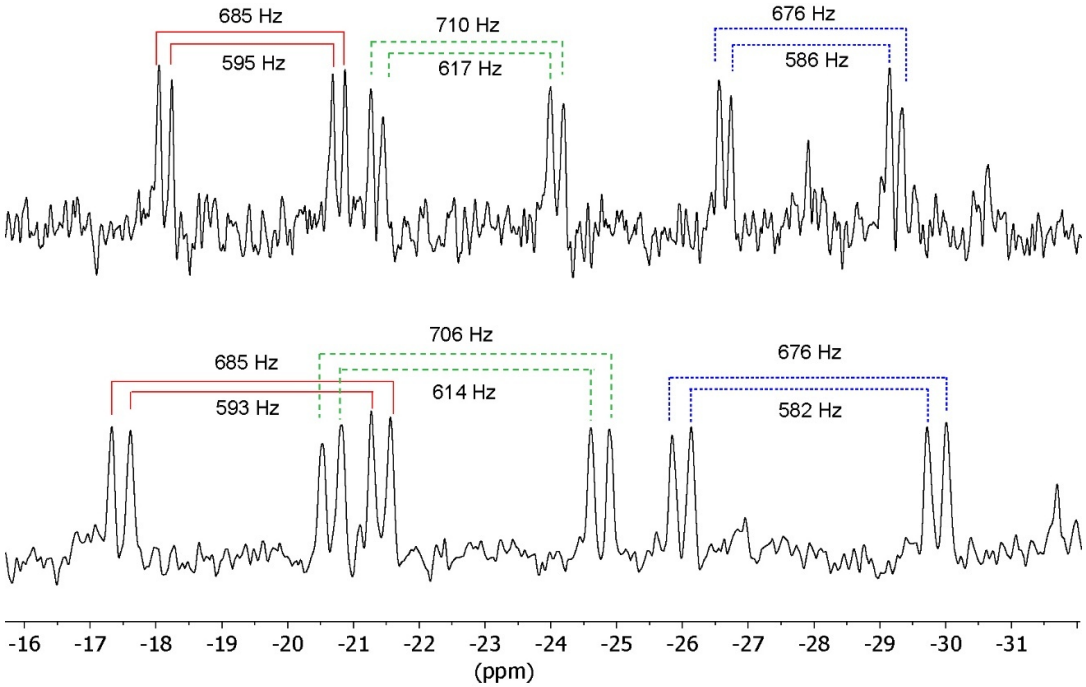

Figure S34. $^{31}P\{^{1}H\}$ NMR spectra (DMSO-d_6) of **Zr-P_2N_2-Ag** measured at 243 MHz (top) and 162 MHz (bottom).

Mass spectrometry and NMR spectroscopy analyses of Zr-P_2N_2-Ag

ESI-MS analysis was performed using an acetonitrile solution of **Zr-P_2N_2-Ag**. ^{1}H and ^{31}P NMR spectra of **Zr-P_2N_2-Ag** were measured in CD_3CN to verify the stability of the cage in this solvent (Figure S36). The ^{31}P NMR spectrum shows three sets of Ag–P resonances in a 1:1:1 ratio, which is consistent with X-ray structure showing the presence of the hexasilver cage. Two of the signals are centered at -25 and -28 ppm with $^{1}J_{Ag–P}$ values in the 615-714 Hz range. These chemical shifts and coupling constants are largely unchanged from those observed in DMSO-d_6, suggesting that the Ag_2(μ-Cl) groups remain intact. However, a new downfield-shifted resonance appears at -8 ppm with significantly smaller $^{1}J_{Ag–P}$ coupling constants (292-336 Hz). This new signal is assigned to the symmetric $(Ag1)_2$ species which undergoes loss of bridging DMSO ligands.[6,7] These findings support retention of the hexasilver core in acetonitrile solvent but imply some loss/exchange of solvent molecules.

The ESI-MS spectrum of **Zr-P_2N_2-Ag** in acetonitrile (Figure S35) reveals an intense mass signal centered at m/z = 1716.99 amu with z = +2. Data fitting and simulation suggest two plausible formulas (**A** and **B**) resulting from loss of coordinated DMSO molecules and association with solvent or other adventitious species. Ion **A** (m/z = 1717.22 amu, z = +2) is simulated as a CN^- adduct, the presence of which may stem from trace HCN present in the acetonitrile solvent.[8] Simulated ion **B** (m/z = 1716.77 amu, z = +2) results from the loss of the two bridging Cl^- ligands along with the association of H_2O and CH_3CN solvent molecules. The simulated mass signals for both ions are shifted slightly from the experimental data, but importantly, no reasonable match for the mass or isotopic distribution could be found for alternative ion compositions with loss off Ag^+ species.

MALDI-TOF mass spectrometry was performed to help resolve the ambiguity of the ESI-MS data (Figure S37). **Zr-P_2N_2-Ag** was dissolved in DMSO and spotted with a DCTB matrix solution. The resulting spectrum shows several weak mass signals in the 1751-1887 amu range. Due to the poor resolution, we were unable to definitively identify the most abundant mass for each signal. Nevertheless, mass and charge of the signals indicate that they correspond to adducts of the parent **Zr-P_2N_2-Ag** cage, and we are able to fit the data with plausible ion formulas. The broad signal at m/z = ~1884.393 amu closely matches simulated ions **A** (m/z = 1886.754 amu, z = +2) and **B** (m/z = 1885.802 amu, z = +2) which are adducts of the parent cage containing DMSO, H_2O, or DCTB molecules. Previous literature reports support the formation of adducts with the DCTB matrix molecule.[9,10] Signals at m/z = ~1820.618 and ~1749.528 amu are well-represented by simulated ions **C** and **D** with varying association of DMSO and water molecules.

Although there is some ambiguity in the ESI-MS and MALDI-TOF data for **Zr-P_2N_2-Ag**, the cumulative evidence supports the lantern-type, hexasilver structure of bulk **Zr-P_2N_2-Ag**.

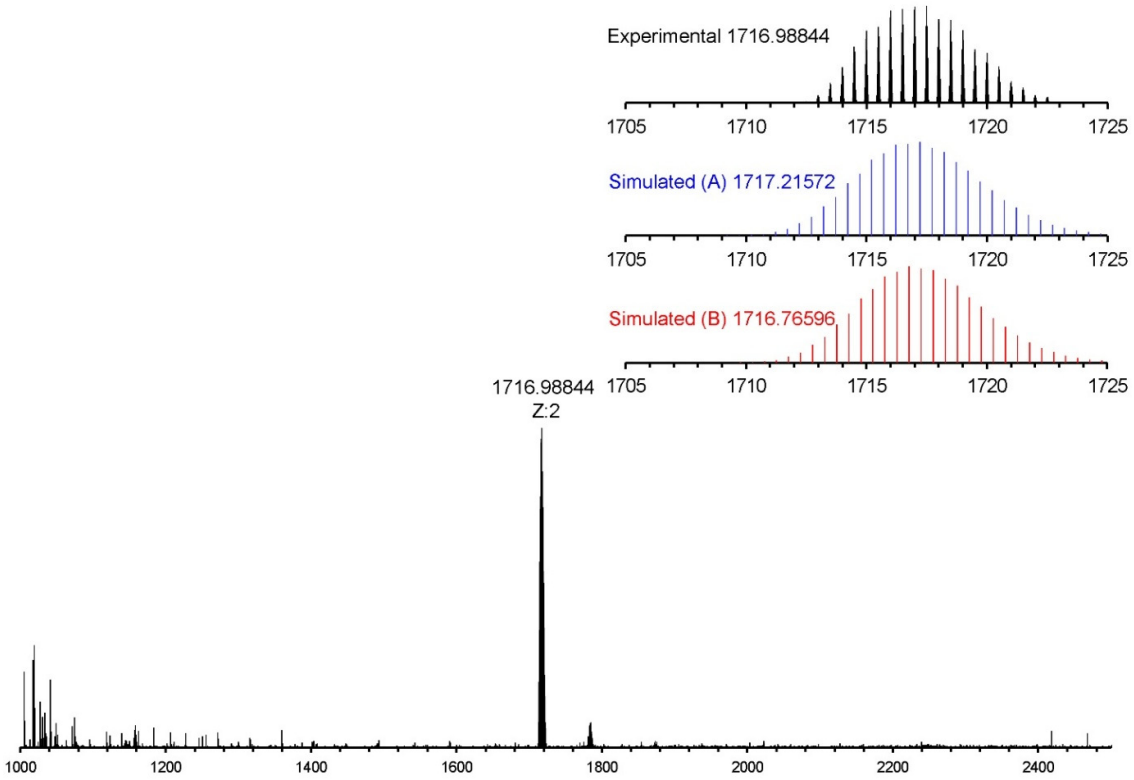

Assignments	m/z experimental	m/z simulated
A $(C_{121}H_{111}Ag_6Cl_2N_7O_{20}P_6Zr_6)^{2+}$ $\{[(ZrCp)_3O_3(OH)][(ZrCp)_3O_2(OH)_2](P_2N_2)_3(Ag)_6(Cl)_2(CN)\}^{2+}$	1716.98844	1717.21572
B $(C_{124}H_{116}Ag_6N_8O_{21}P_6Zr_6)^{2+}$ $\{[(ZrCp)_3O_4]_2(P_2N_2)_3(Ag)_6(H_2O)_2(MeCN)_2\}^{2+}$		1716.76596

Sample was dissolved in acetonitrile and measured in positive mode with m/z range of 200-3000 amu.

Figure S35. Simulated and experimental ESI-MS spectra of **Zr-P_2N_2-Ag**.

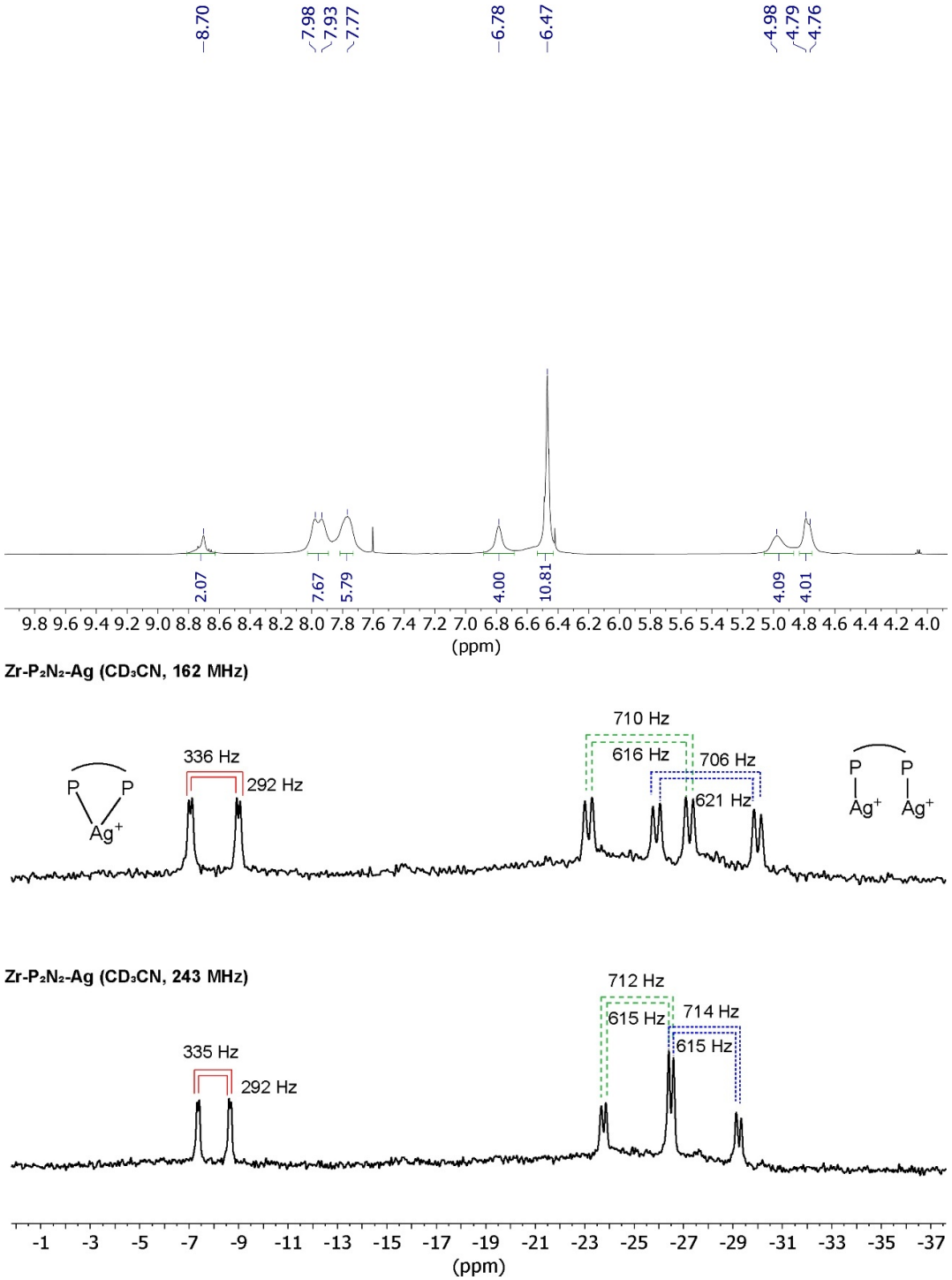

Figure S36. ^{1}H and $^{31}P\{^{1}H\}$ NMR spectra of **Zr-P_2N_2-Ag** in CD_3CN.

(600 MHz, 162 MHz and 243 MHz)

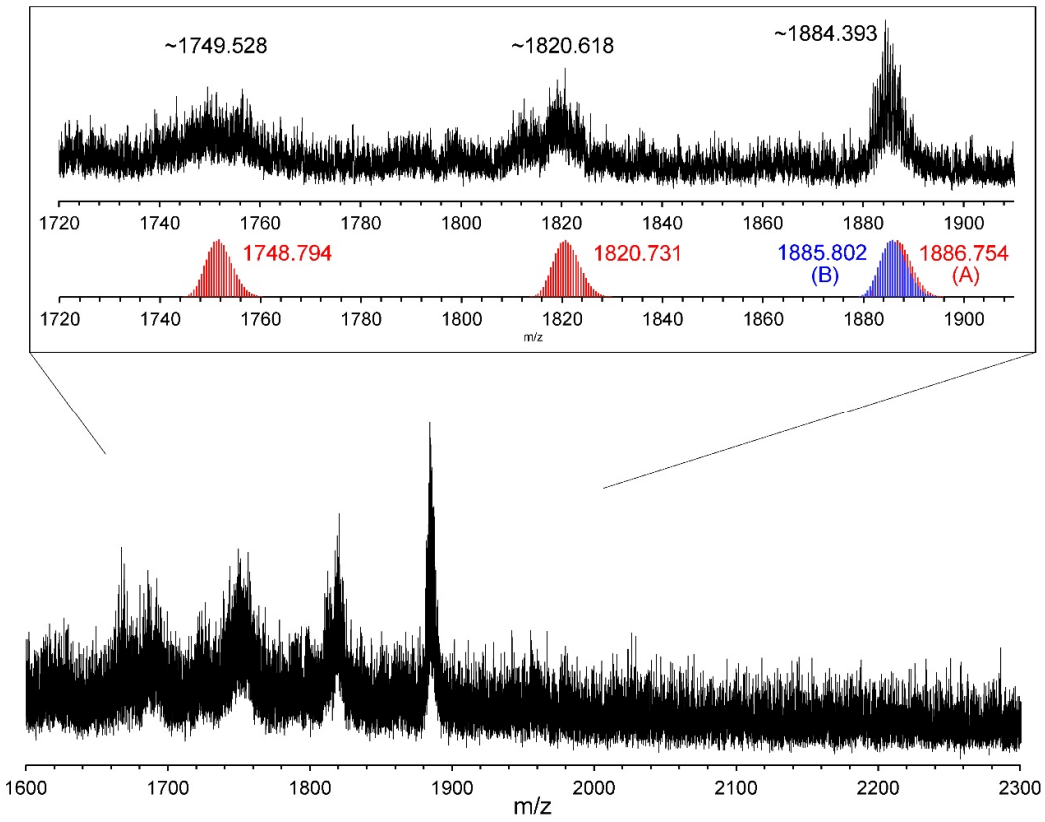

Assignments	m/z experimental	m/z simulated
A $(C_{128}H_{140}Ag_6Cl_2N_6O_{27}P_6S_4Zr_6)^{2+}$ $\{[(ZrCp)_3O_3(OH)]_2(P_2N_2)_3(Ag)_6(Cl)_2(DMSO)_4(H_2O)_3\}^{2+}$	~1884.393	1886.754
B $(C_{139}H_{138}Ag_6Cl_2N_8O_{23}P_6SZr_6)^{2+}$ $\{[(ZrCp)_3O_3(OH)]_2(P_2N_2)_3(Ag)_6(Cl)_2(DCTB)(DMSO)(H_2O)_2\}^{2+}$ (DCTB = matrix, $C_{17}H_{18}N_2$)		1885.802
C $(C_{126}H_{128}Ag_6Cl_2N_6O_{23}P_6S_3Zr_6)^{2+}$ $\{[(ZrCp)_3O_3(OH)]_2(P_2N_2)_3(Ag)_6(Cl)_2(DMSO)_3\}^{2+}$	~1820.618	1820.731
D $(C_{122}H_{118}Ag_6Cl_2N_6O_{22}P_6SZr_6)^{2+}$ $\{[(ZrCp)_3O_3(OH)]_2(P_2N_2)_3(Ag)_6(Cl)_2(DMSO)(H_2O)\}^{2+}$	~1749.528	1751.722

Figure S37. Simulated and experimental MALDI-TOF spectra of **Zr-P_2N_2-Ag**.

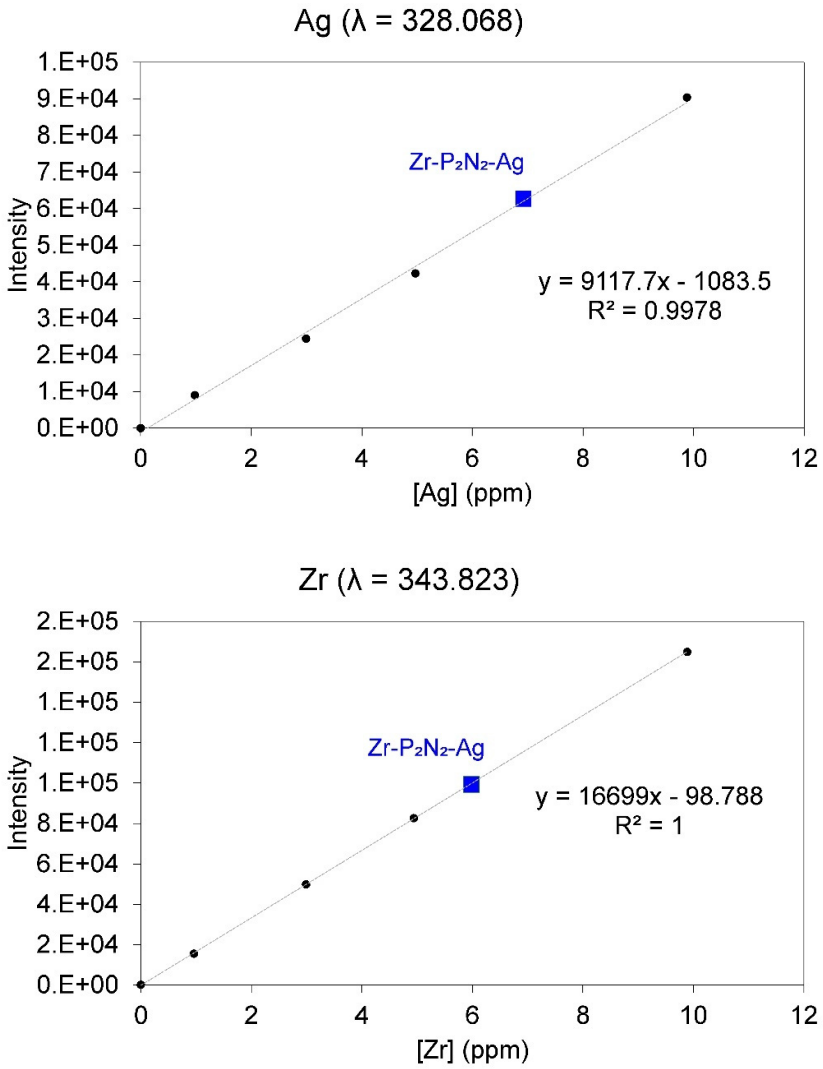

Figure S38. ICP-OES calibration curves and data for **Zr-P_2N_2-Ag**.

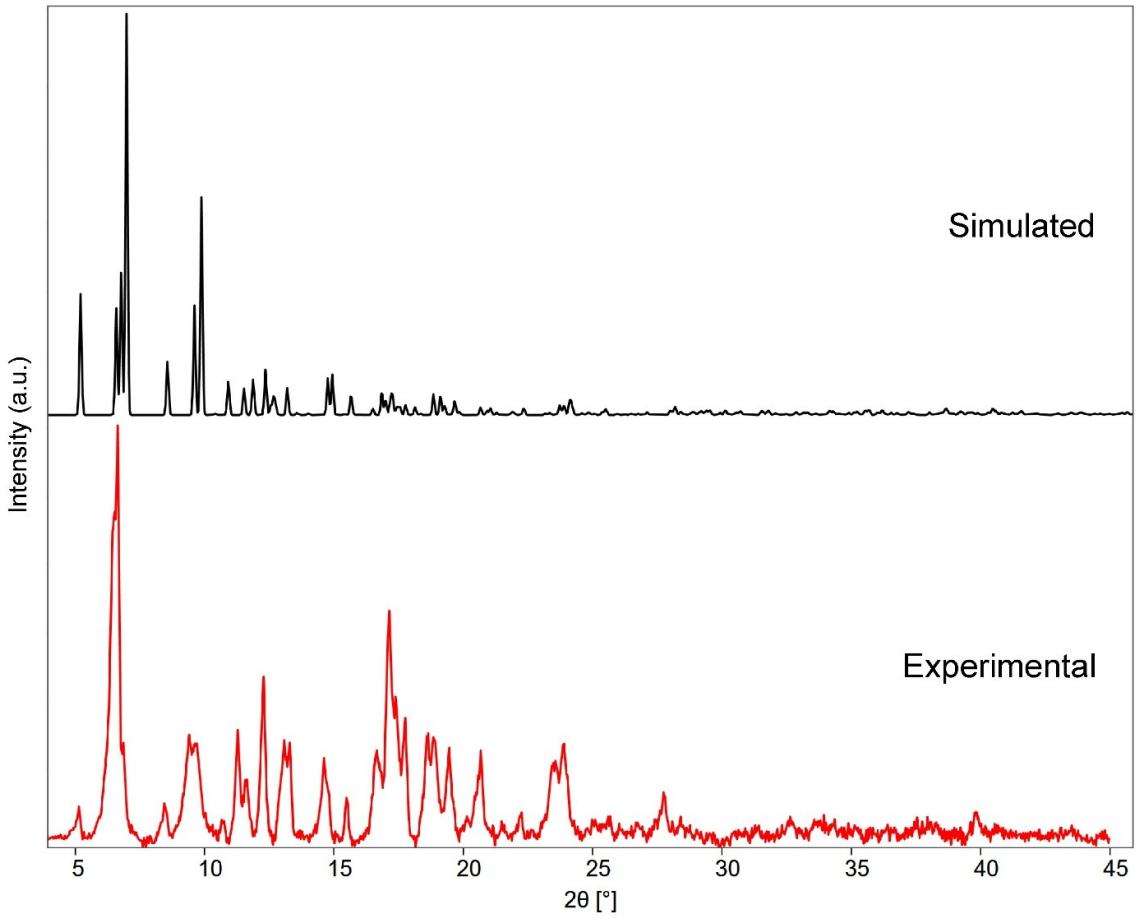

Figure S39. Simulated and experimental PXRD patterns of **Zr-P_2N_2**.

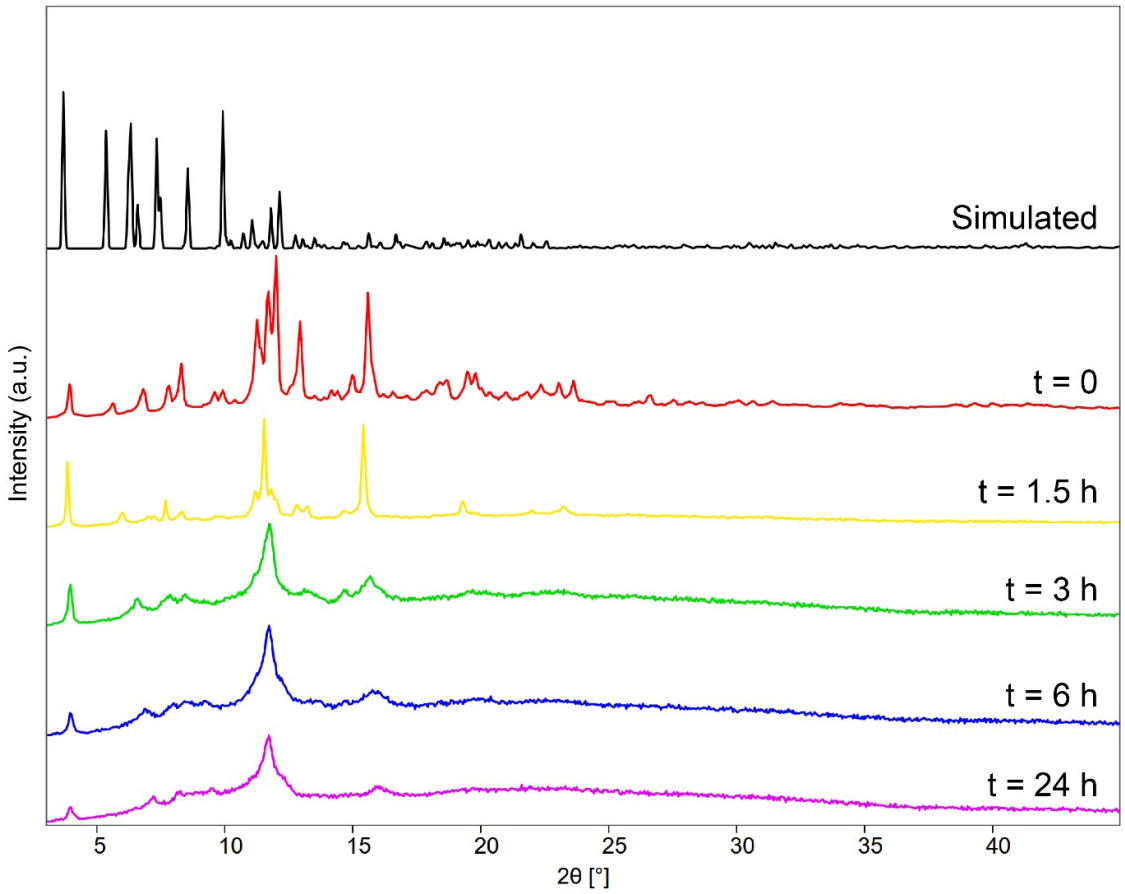

Figure S40. Simulated and experimental PXRD patterns of **Zr-P_2N_2-$PdCl_2$**.

The t=0 sample was obtained from a direct solvothermal reaction and isolated without washing. The crystalline solid was minimally dried and carefully ground to provide uniform samples for PXRD analysis. Despite these precautions, the experimental PXRD pattern does not closely match that simulated from the single crystal structure. Additional PXRD patterns were recorded upon exposing the sample to ambient conditions over the course of 24 hours. These data reveal a rapid phase change and decreased crystallinity, which can be attributed to lattice transformation caused by desolvation.

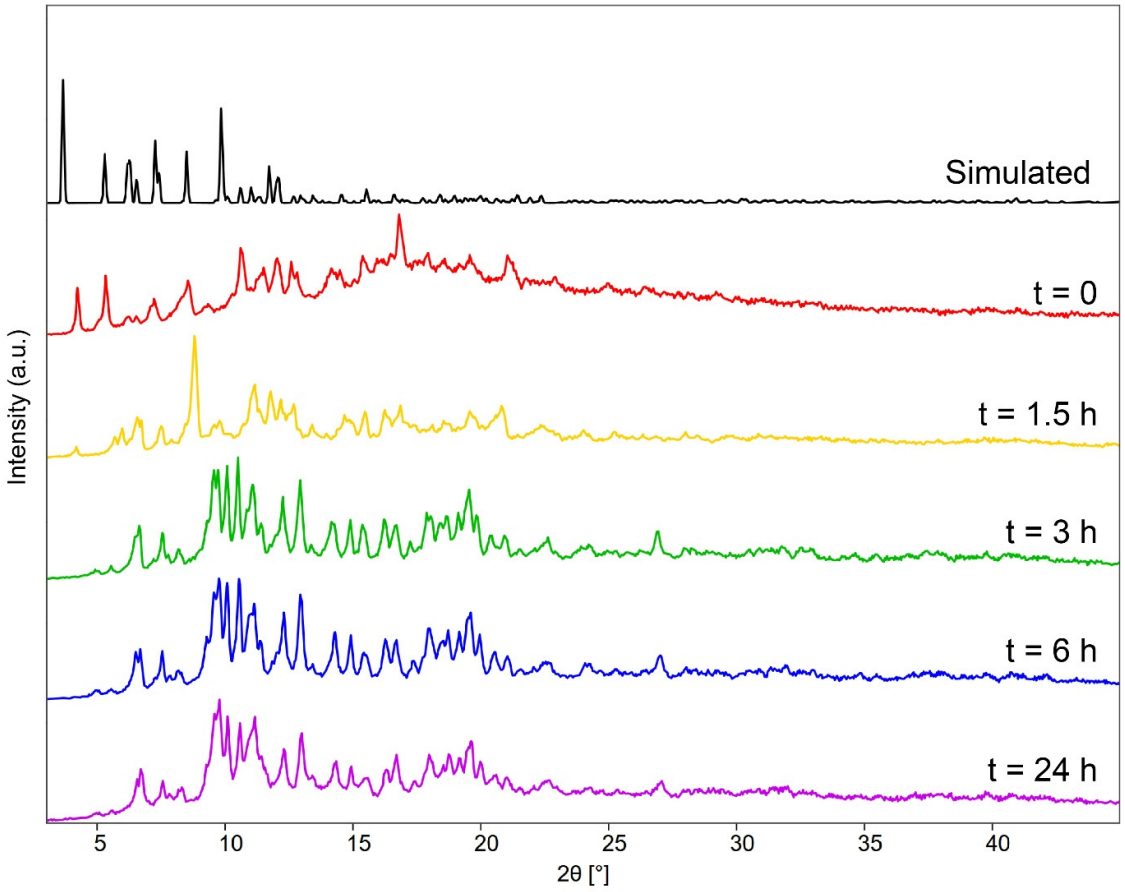

Figure S41. Simulated and experimental PXRD patterns of **Zr-P_2N_2-$PtCl_2$**.

The t=0 sample was obtained from a direct solvothermal reaction and isolated without washing. The crystalline solid was minimally dried and carefully ground to provide uniform samples for PXRD analysis. Despite these precautions, the experimental PXRD pattern does not closely match that simulated from the single crystal structure. Additional PXRD patterns were recorded upon exposing the sample to ambient conditions over the course of 24 hours. These data reveal a rapid phase change, which can be attributed to lattice transformation caused by desolvation.

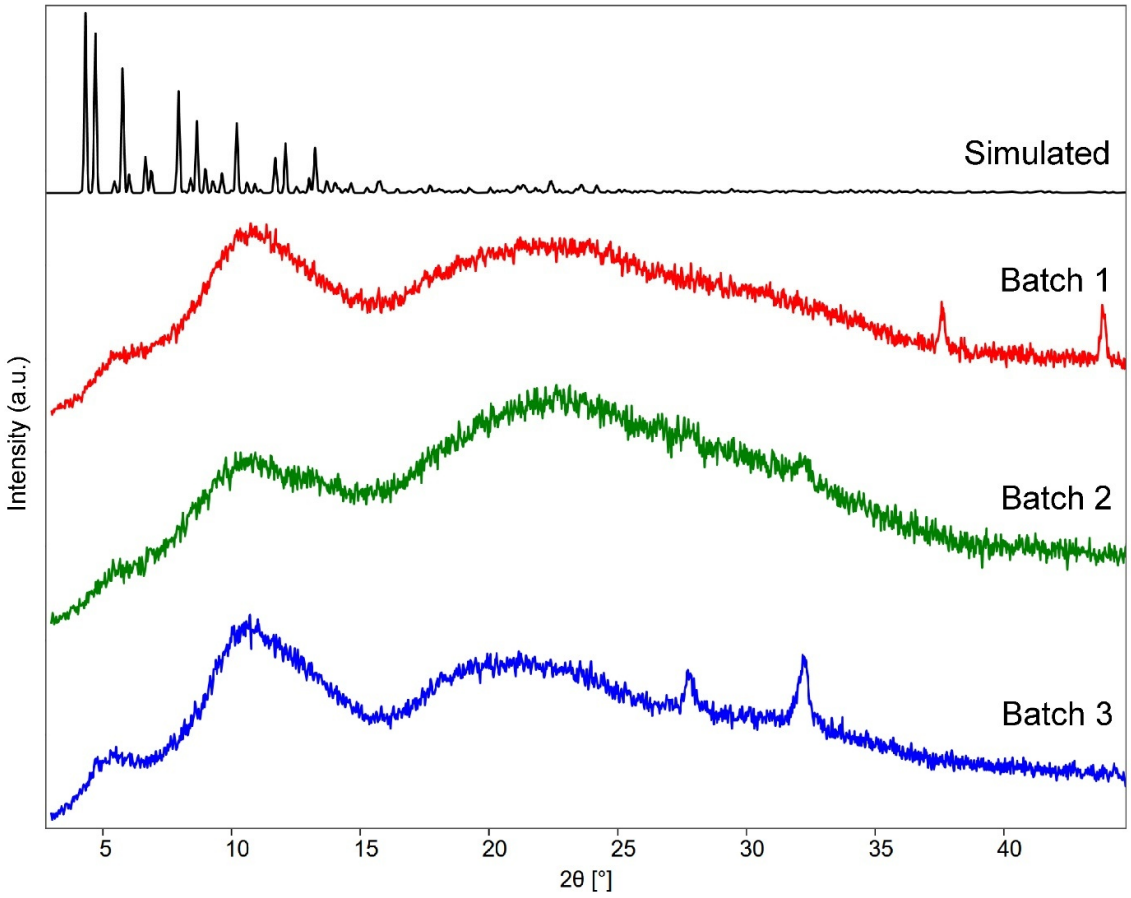

Figure S42. Simulated and experimental PXRD patterns of **Zr-P_2N_2-Ag**.

PXRD patterns were collected for three independently synthesized batches of **Zr-P_2N_2-Ag**. Despite careful sample handling and preparation, the data reveal largely amorphous samples. These results suggest that crystalline **Zr-P_2N_2-Ag** is highly sensitive to exposure to ambient conditions and undergoes decomposition or desolvation to an amorphous phase.

References

1 G. A. Taggart, A. Guliyeva, K. Kim, G. P. A. Yap, D. J. Pochan, T. H. Epps and E. D. Bloch, *J. Phys. Chem. C*, 2023, **127**, 2379–2386.

2 M. G. Sullivan, H. K. Welgama, M. R. Crawley, A. E. Friedman and T. R. Cook, *Chem. Mater.*, 2024, **36**, 567–574.

3 U. Warzok, M. Marianski, W. Hoffmann, L. Turunen, K. Rissanen, K. Pagel and C. A. Schalley, *Chem. Sci.*, 2018, **9**, 8343–8351.

4 E. Benchimol, B.-N. T. Nguyen, T. K. Ronson and J. R. Nitschke, *Chem. Soc. Rev.*, 2022, **51**, 5101–5135.

5 K. Matsumoto, S. Kusaba, Y. Tanaka, Y. Sei, M. Akita, K. Aritani, M. Haga and M. Yoshizawa, *Angew. Chem., Int. Ed.*, 2019, **58**, 8463–8467.

6 K. Plevová, L. J. Prieto Pabon, M. Gaysinski, S. Poulain-Martini and V. Michelet, *Chempluschem*, 2022, **87**, e202200217.

7 B. Attenberger, M. El Sayed Moussa, T. Brietzke, V. Vreshch, H. Holdt, C. Lescop and M. Scheer, *Eur. J. Inorg. Chem.*, 2015, **2015**, 2934–2938.

8 V. K. Kadambar, B. S. Kushwah, R. Gupta, D. Sunny, H. Vachhani, J. Young and L. Bajpai, *Org. Process Res. Dev.*, 2024, **28**, 4059–4068.

9 X. Lou, B. F. M. de Waal, J. L. J. van Dongen, J. A. J. M. Vekemans and E. W. Meijer, *J. Mass Spectrom.*, 2010, **45**, 1195–1202.

10 X. Lou, M. Fransen, P. J. M. Stals, T. Mes, R. Bovee, J. J. L. van Dongen and E. W. Meijer, *J. Am. Soc. Mass Spectrom.*, 2013, **24**, 1405–1412.